

## Molecular gas in a gravitationally lensed galaxy group at $z = 2.9$

JEFF SHEN,<sup>1,2</sup> ALLISON W. S. MAN,<sup>1,3</sup> JOHANNES ZABL,<sup>4,5</sup> ZHI-YU ZHANG,<sup>6,7</sup> MIKKEL STOCKMANN,<sup>8,9</sup>  
GABRIEL BRAMMER,<sup>8,9</sup> KATHERINE E. WHITAKER,<sup>8,10</sup> AND JOHAN RICHARD<sup>4</sup>

<sup>1</sup>*Dunlap Institute for Astronomy and Astrophysics, University of Toronto, 50 St George Street, Toronto ON, M5S 3H4, Canada*

<sup>2</sup>*Department of Statistical Sciences, University of Toronto, 100 St George Street, Toronto ON, M5S 3G3, Canada*

<sup>3</sup>*Department of Physics & Astronomy, University of British Columbia, 6224 Agricultural Road, Vancouver, BC V6T 1Z1, Canada*

<sup>4</sup>*Univ Lyon, Univ Lyon1, Ens de Lyon, CNRS, Centre de Recherche Astrophysique de Lyon UMR5574, F-69230, Saint-Genis-Laval, France*

<sup>5</sup>*Institute for Computational Astrophysics and Department of Astronomy & Physics, Saint Mary's University, 923 Robie Street, Halifax, Nova Scotia, B3H 3C3, Canada*

<sup>6</sup>*School of Astronomy and Space Science, Nanjing University, Nanjing 210093, People's Republic of China*

<sup>7</sup>*Key Laboratory of Modern Astronomy and Astrophysics (Nanjing University), Ministry of Education, Nanjing 210093, People's Republic of China*

<sup>8</sup>*Cosmic Dawn Center (DAWN)*

<sup>9</sup>*Niels Bohr Institute, University of Copenhagen, Jagtvej 128, DK-2100 Copenhagen, Denmark*

<sup>10</sup>*Department of Astronomy, University of Massachusetts, 710 North Pleasant Street, Amherst, MA 01003, USA*

(Received 2020 October 27; Revised 2021 May 17; Accepted 2021 May 20)

### ABSTRACT

Most molecular gas studies of  $z > 2.5$  galaxies are of intrinsically bright objects, despite the galaxy population being primarily "normal" galaxies with less extreme star formation rates. Observations of normal galaxies at high redshift provide a more representative view of galaxy evolution and star formation, but such observations are challenging to obtain. In this work, we present ALMA  $^{12}\text{CO}(J=3\rightarrow 2)$  observations of a sub-millimeter selected galaxy group at  $z = 2.9$ , resulting in spectroscopic confirmation of seven images from four member galaxies. These galaxies are strongly lensed by the MS 0451.6–0305 foreground cluster at  $z=0.55$ , allowing us to probe the molecular gas content on levels of  $10^9 - 10^{10} M_{\odot}$ . Four detected galaxies have molecular gas masses of  $(0.2 - 13.1) \times 10^{10} M_{\odot}$ , and the non-detected galaxies have inferred molecular gas masses of  $< 8.0 \times 10^{10} M_{\odot}$ . We compare these new data to a compilation of 546 galaxies up to  $z = 5.3$ , and find that depletion times decrease with increasing redshift. We then compare the depletion times of galaxies in overdense environments to the field scaling relation from the literature, and find that the depletion time evolution is steeper for galaxies in overdense environments than for those in the field. More molecular gas measurements of normal galaxies in overdense environments at higher redshifts ( $z > 2.5$ ) are needed to verify the environmental dependence of star formation and gas depletion.

*Unified Astronomy Thesaurus concepts:* Galaxy evolution (594); High-redshift galaxies (734); High-redshift galaxy clusters (2007); Star formation (1569); Strong gravitational lensing (1643)

### 1. INTRODUCTION

Molecular gas is the fuel for star formation and is consequently a key parameter in determining how galaxies evolve. Although we have a deep understanding of the galaxy populations of today (see review by Blanton & Moustakas 2009), observations of distant galaxies are important for us to infer how galaxies formed and evolved (Tacconi et al. 2020). A crucial cosmic epoch is the peak of cosmic star formation history from  $z \approx 1 - 3$  when roughly half of the stars in the present-day Universe formed (Shapley 2011; Madau & Dickinson 2014).

High-redshift galaxies have historically been difficult to detect, relative to local galaxies, due to their distance. As such, detections of molecular gas in high-

$z$  star-forming galaxies are heavily biased towards the most extremely star-forming galaxies, which harbour copious amounts of molecular gas (e.g., [Walter et al. 2004](#); [Carilli et al. 2010](#); [Danielson et al. 2010](#); [Riechers et al. 2010a](#); [Combes et al. 2012](#); [Spilker et al. 2015](#); [Miller et al. 2018](#); [Tadaki et al. 2018](#); [Ciesla et al. 2020](#); [Spingola et al. 2020](#)).

The vast majority of galaxies are not as strongly star forming as submillimeter galaxies (SMGs; [Madau & Dickinson 2014](#)). It is thus vital to characterize the molecular gas of distant "normal" galaxies in order to understand the representative mode of star formation. Significant progress toward this goal has been made since the advent of the Atacama Large Millimeter/submillimeter Array (ALMA), whose sensitivity has enabled studies that probe faint carbon monoxide emissions (CO, a common tracer for molecular gas) in distant galaxies (e.g., review by [Hodge & da Cunha 2020](#)). However, obtaining CO detections of normal galaxies at  $z > 2$  remains a challenge.

To date, only a few galaxy clusters with molecular gas mass measurements have spectroscopic confirmations, with the majority of them at  $z < 2.5$  ([Noble et al. 2017](#); [Rudnick et al. 2017](#); [Hayashi et al. 2018](#)). These cluster galaxies also present a range of results on the gas content, with gas fractions ( $f_{gas} = M_{gas}/(M_{gas} + M_*)$ ), where  $M_{gas}$  is the gas mass and  $M_*$  is the stellar mass) and depletion times ( $t_{depl} = M_{gas}/SFR$ , where SFR is the star formation rate) varying by over an order of magnitude. In contrast, protoclusters discovered at  $z > 4$  all contain massive starburst galaxies totalling star formation rates (SFRs) of over  $6000 M_{\odot} \text{ yr}^{-1}$  in the entire protocluster ([Miller et al. 2018](#); [Oteo et al. 2018](#)), which may suggest that the  $z = 2 - 4$  is a time of transition in the star formation of galaxy protoclusters.

A relevant and ongoing discussion relating to molecular gas in high-redshift galaxies is the environmental dependence of molecular gas properties like the gas fraction and depletion time. Generally, a high-density environment means that a higher molecular gas content, and thus star formation, would be expected ([Schmidt 1959](#)). However, the dense environment also promotes more interactions between galaxies and facilitates processes such as ram-pressure stripping and strangulation which would reduce a galaxy's gas content during their infall towards the cluster center ([Mo et al. 2010](#)). Some studies find evidence of higher molecular gas fractions in clusters than field scaling relations ([Noble et al. 2017](#); [Hayashi et al. 2018](#); [Gómez-Guijarro et al. 2019](#); [Tadaki et al. 2019](#), for galaxies with stellar mass  $10.5 < \log(M_*/M_{\odot}) < 11.0$ ). On the other hand, there is also evidence for similar molecular gas fractions

between coeval cluster and field galaxies ([Dannerbauer et al. 2017](#); [Lee et al. 2017](#); [Stach et al. 2017](#)), and for the presence of massive galaxies, primarily near the center of clusters, which contain extremely low molecular gas fractions ([Wang et al. 2018](#); [Zavala et al. 2019](#)). This molecular gas deficiency is attributed to quenching mechanisms which inhibit gas accretion or cooling; alternatively, the molecular gas may have been rapidly consumed or expelled ([Man & Belli 2018](#), and references therein). However, most of these studies on the molecular gas content of cluster galaxies have been limited to  $z < 2.5$  ([Tacconi et al. 2020](#)). Obtaining higher redshift observations of protocluster galaxies would shed light on the impact of an overdense environment on molecular gas, and how that evolves with time.

The use of strong gravitational lensing makes it possible to detect galaxies that are otherwise too faint for spectroscopic follow up. Previous studies have found success using lensing as a tool to probe galaxies with relatively low SFRs ( $\ll 1000 M_{\odot} \text{ yr}^{-1}$ ), which are considered to be "normal" at  $z > 2$  ([Saintonge et al. 2013](#); [Dessauges-Zavadsky et al. 2015, 2017](#)).

In this paper, we present  $^{12}\text{CO}(J=3 \rightarrow 2)$  observations of a group of interacting normal star-forming galaxies at  $z \approx 2.9$  in a giant sub-millimeter arc ([Borys et al. 2004](#)) lensed by the MS 0451.6-0305 foreground cluster ([MacKenzie et al. 2014](#)). The group is composed of nine sources, labeled Gals. 1-9 as in [MacKenzie et al. \(2014\)](#). We note that Gal. 9 is a foreground galaxy, and do not present an analysis of its CO content in this work. The total SFR, as derived from far-infrared (FIR) luminosity, of  $450 \pm 50 M_{\odot} \text{ yr}^{-1}$  for the entire group is far lower than the SFR of known protoclusters at comparable redshifts; the protoclusters in [Oteo et al. \(2018\)](#), [Miller et al. \(2018\)](#), [Wang et al. \(2018\)](#), [Gómez-Guijarro et al. \(2019\)](#), and [Zavala et al. \(2019\)](#) have SFR that range from  $1400 M_{\odot} \text{ yr}^{-1}$  to over  $6000 M_{\odot} \text{ yr}^{-1}$ . Several of the background sub-millimeter (submm) sources in the group are multiply imaged due to the lensing, and have been observed at optical and radio wavelengths ([Borys et al. 2004](#); [Berciano Alba et al. 2007](#); [Berciano Alba et al. 2010](#); [Zitrin et al. 2010](#); [Jauzac et al. 2020](#)).

The environment, redshift, and SFR of the lensed sources make them valuable for investigating star formation in early protocluster galaxies. Using data from ALMA, we examine the molecular gas content of the sources and compare our results to a compilation of high-redshift galaxies. Using this compiled sample, we also discuss the impact of the environment and the redshift evolution of the depletion time, an important quantity in the discussion of molecular gas underpinning the future star formation potential of galaxies.

The layout of this paper is as follows. In Section 2 we describe the observations and data reduction. In Section 3 we analyze the CO observations and describe the calculation of molecular gas masses of the sources. In Section 4 we discuss our findings in the context of high-redshift galaxy evolution, compare the gas properties of our sources against a compilation of primarily CO-detected high-redshift galaxies, and consider the uncertainties in our results. A summary of this paper is presented in Section 5.

Throughout this paper, we assume a Kroupa (2001) initial mass function (IMF), a flat  $\Lambda$ CDM cosmology, a Hubble constant at  $z = 0$  of  $H_0 = 70 \text{ km s}^{-1} \text{ Mpc}^{-1}$ , and a density of non-relativistic matter at  $z = 0$  of  $\Omega_M = 0.3$ , in units of the critical density. At  $z = 2.9$ ,  $1''$  corresponds to 7.78 kpc.

## 2. OBSERVATIONS

### 2.1. ALMA

Observations of MS 0451.6–0305 were performed with the ALMA 12m array under the project code 2017.1.00616.S (PI: Allison Man). The 41 antennas were arranged in a compact configuration with baselines ranging from 14 m to 783 m. The total on-source integration time was 64.08 minutes over two consecutive execution blocks on 12–13 March 2018. The precipitable water vapor during the observations was about 2.94–3.19 mm. J0423-0120 was used as a flux and bandpass calibrator while J0501-0159 was used for phase calibration. The pointings were centered on Gal. 1.b following the MacKenzie et al. (2014) naming convention. We used ALMA Band 3 in a mixed spectral setup to target the  $^{12}\text{CO}(J=3\rightarrow 2)$  transition ( $\nu_{\text{rest}} = 345.796 \text{ GHz}$ ) at  $z \approx 2.9$ , the redshift of the lensed group. A spectral window was centered on 88.136 GHz covering a bandwidth of 1.875 GHz with 240 channels. The native channel width is thus  $26.6 \text{ km s}^{-1}$ .

The data were calibrated with the Common Astronomy Software Package (CASA version 5.4.0; McMullin et al. 2007) with pipeline version 42030. The data cube was imaged with natural weighting to optimize the signal-to-noise (SNR) of compact sources. The resulting synthesized beam is  $1.81'' \times 1.28''$  corresponding to  $14.08 \text{ kpc} \times 9.96 \text{ kpc}$  at  $z = 2.9$ , with a position angle of  $-64.3^\circ$ . We further bin the cube with the CLEAN task (Högbom 1974) to a channel width of  $100 \text{ km s}^{-1}$  to improve SNR. The moment maps in Figure 1 are created with the non-primary-beam corrected cube, and the spectra are extracted from the primary-beam corrected cube. We measure different noises for each source, as the sources are spread out over the field-of-view.

### 2.2. HST

*Hubble Space Telescope (HST)* wide-field imaging observations of MS 0451.6–0305 are available in six optical or near-infrared filters (Egami et al. 2010; Jauzac et al. 2020). The main purposes of using *HST* images for this work is to create an RGB image (Figure 1) and to identify the source positions for spectral extraction (Section 3.2). For these purposes, we use the deepest optical image (F814W) taken with the Advanced Camera for Surveys (ACS), and the two near-infrared images (F110W and F160W) taken with the Wide-Field Camera 3 (WFC3). Three epochs of ACS/F814W images are available (program IDs: 9836, 10493, 11591) for a total exposure time of 11438 s. The WFC3 F110 and F160W images each has exposure time of 2612 s and 2412 s, respectively (program ID 11591). The individual exposures were retrieved from the Mikulski Archive for Space Telescopes website<sup>1</sup>. For each “visit” (i.e., a set of exposures of a target taken with an instrument and filter combination at each epoch), the absolute astrometry is aligned to stars in the *Gaia* DR2 catalog (Gaia Collaboration et al. 2018). The alignment of the *HST* images is done with seven *Gaia* DR2 stars within the *HST* footprint, six of which are matched to better than 20 mas. We have also compared the positional offsets of stars in the Pan-STARRS catalog PS 1 (Chambers et al. 2019), which has a higher source density but lower astrometric precision than *Gaia*. For the 55 stars from Pan-STARRS PS1, the residual offset is 43 mas. Both of these values are smaller than the 60 mas size of one *HST* pixel. Standard imaging calibration procedure were applied with the *grizli* analysis software (Brammer 2019)<sup>2</sup>. The exposures per filter are combined into a mosaic and drizzled onto a common pixel scale of  $0.06''$ .

## 3. ANALYSIS AND RESULTS

### 3.1. Star Formation Rates

The SFRs used in this paper are obtained from MacKenzie et al. (2014), who employed a forward-modelling approach in combination with Markov Chain Monte Carlo methods to simultaneously deblend and fit spectral energy distributions (SEDs) to the source galaxies whose emissions are blended together in a giant submillimeter arc. They made use of  $450 \mu\text{m}$  and  $850 \mu\text{m}$  data from the Submillimetre Common-User Bolometer Array (SCUBA)-2, as well as *Herschel* Spectral and Photometric Imaging Receiver (SPIRE) and Photodetecting Array Camera and Spectrometer (PACS) data.

<sup>1</sup> <https://archive.stsci.edu>

<sup>2</sup> <https://github.com/gbrammer/grizli>

The locations of *HST* candidate counterparts are used as priors for the source of submm emissions during the SED fitting. By integrating the resulting SEDs, they obtain intrinsic FIR luminosities, which were converted to SFRs with the relation

$$\text{SFR} = 1.49 \times 10^{-10} \text{ M}_{\odot} \text{ yr}^{-1} \text{ L}_{\text{FIR}} \text{ L}_{\odot}^{-1} \quad (1)$$

from [Murphy et al. \(2011\)](#) with the assumption that UV radiation is completely absorbed by dust and reradiated at longer wavelengths. We refer the reader to [MacKenzie et al. \(2014\)](#) for a more detailed description of the procedures.

### 3.2. Spectrum Extraction

High-redshift galaxies can have slight offsets between their optical/near-infrared (IR) and submillimeter positions due to different astrometry reference systems or intrinsic offsets between stars and gas. In our data, we note offsets in the locations of the *HST* peaks and the corresponding ALMA peaks. We explore reasons for the observed offsets in Section 4.4 and argue that the offsets are intrinsic, rather than astrometric.

We recalculate the *HST* locations by first creating an *HST* RGB image with the F160W, F110W, and F814W filters as the red, green, and blue channels, respectively. We then use a combination of cropping and brightness masking to isolate each source as best as possible before fitting 2D Gaussians to each source using a least squares algorithm ([Levenberg 1944](#)) and taking the center as the *HST* location. These new locations are given in Table 1. The *HST* images are aligned to the *Gaia* astrometric data and differ from the positions given in [MacKenzie et al. \(2014\)](#) by an average of  $0.344''$ . This difference is due to the different astrometry reference systems as well as the filters used for locating the sources.

For each detected galaxy, the ALMA peak was calculated by applying the same 2D Gaussian fitting technique used to find the *HST* locations to the moment zero maps (see below for a description of how these are obtained). The centers of the best-fit Gaussians are also reported in Table 1. The offset between the *HST* and ALMA peaks for detected galaxies, where the CO emission is detected and both locations are unambiguous, are given in Table 2.

For each galaxy with reported offsets, both the *HST* and ALMA positions are passed through the [MacKenzie et al. \(2014\)](#) lens model along with their uncertainties to obtain corresponding positions and uncertainties on the source plane. From these source plane positions, we are able to calculate the offset and position angle on the source plane. These offsets also reported in Table 2, range from  $0.14''$  to  $0.33''$  and are statistically significant for all five sources.

Because of the *HST*–ALMA offsets, we do not extract spectra using apertures centered on the *HST* positions. Rather, we adopt the following procedure to identify the optimal extraction apertures for the  $^{12}\text{CO}(J=3\rightarrow 2)$  spectra of each galaxy. We note that the non-detected galaxies have a different extraction procedure described later in the subsection.

For each source, we use an initial  $6'' \times 6''$  extraction to create a velocity-integrated flux map (also known as moment zero map) centered at the *HST* position. This is done by integrating the velocity channels ranging from  $-200 \text{ km s}^{-1}$  to  $+200 \text{ km s}^{-1}$  around the peak of the  $^{12}\text{CO}(J=3\rightarrow 2)$  emission as identified from the 1D spectrum, which is calculated by spatially integrating the same extraction. Contours of the local rms noise are also calculated and overplotted. This noise is calculated by fitting a 1D Gaussian to a histogram of a mirrored version of the negative flux values in a  $60'' \times 60''$  moment zero map centered at the source. Examples of moment zero maps and contours are shown in Figure 1, as well as in Appendix B.

The contours are used to optimize the extraction region from which we obtain the spectra. We use these contours to perform a masking procedure, which we repeat at  $0.2\sigma$  increments from  $0\sigma$  to  $5\sigma$ , where  $\sigma$  is the rms noise as calculated previously. First, the primary contour corresponding to a given noise level (e.g.,  $2\sigma$ ) is selected and used to indicate the spatial extent of the CO emission in the original cube. Note that there may be multiple disjoint contours at this noise level; only the *primary* contour which encloses the pixel with the maximum integrated flux is selected. The spectrum is then calculated by integrating the flux over the region within the contour in all channels in the spectral window. The SNR of this spectrum is defined as the flux in the peak channel over the rms flux of the spectrum with the peak channel removed.

Through this iterative process, we define an optimal extraction region (i.e., contour level) which maximizes the SNR of the spectrum. In Figure 1, the optimal extraction region of each source is given by the dashed black line in the moment zero maps, and by the (same) white line in the *HST* cutouts. We note that this procedure is robust with respect to the initial extraction—regardless of the initial cube position or size (given that the source is entirely contained within the cube), the optimal region will be extracted.

Each source was inspected to ensure that there were no false signals due to contributions from nearby sources. Sources with  $\text{SNR} > 3$  as obtained by the described method were classified as a detection. The spectra of the detections, alongside the moment zero maps and

**Table 1.** *HST* and ALMA locations of sources.

Gal	R.A.	R.A. Err.	Dec.	Dec. Err.	R.A.	R.A. Err. <sup>a</sup>	Dec.	Dec. Err. <sup>a</sup>
ID	J2000	arcsec	J2000	arcsec	J2000	arcsec	J2000	arcsec
<i>HST</i>					ALMA <sup>e</sup>			
1.a	04 <sup>h</sup> 54 <sup>m</sup> 13.415 <sup>s</sup>	0.014''	-3° 00' 42.708''	0.028''	...	...	...	...
1.b	04 54 12.643	0.035	-03 01 16.210	0.034	...	...	...	...
1.c	04 54 12.161	0.016	-03 01 21.161	0.016	...	...	...	...
2.a	04 54 13.142	0.009	-03 00 38.114	0.012	...	...	...	...
2.b	04 54 12.565	0.011	-03 01 11.661	0.011	04 <sup>h</sup> 54 <sup>m</sup> 12.537 <sup>s</sup>	0.181''	-03° 01' 12.508''	0.181''
2.c	04 54 11.777	0.042	-03 01 19.872	0.020	04 54 11.841	0.182	-03 01 19.688	0.181
3.a	04 54 13.033	0.009	-03 00 38.943	0.015	...	...	...	...
3.b	04 54 12.670	0.026	-03 01 08.755	0.037	...	...	...	...
3.c	04 54 11.452	0.016	-03 01 21.404	0.016	...	...	...	...
4.a	04 54 12.812	0.009	-03 00 38.957	0.011	...	...	...	...
4.b <sup>b</sup>	...	...	...	...	...	...	...	...
4.c	04 54 11.020	0.014	-03 01 22.074	0.015	...	...	...	...
5.a	04 54 12.793	0.018	-03 00 44.066	0.024	04 54 12.807	0.195	-03 00 44.083	0.199
5.b	04 54 12.665	0.061	-03 01 01.168	0.044	04 54 12.690	0.183	-03 01 01.726	0.183
5.c	04 54 10.911	0.040	-03 01 24.290	0.019	...	...	...	...
6.a <sup>c</sup>	...	...	...	...	...	...	...	...
6.b <sup>c</sup>	...	...	...	...	...	...	...	...
6.c <sup>c</sup>	...	...	...	...	...	...	...	...
7.a <sup>d</sup>	...	...	...	...	04 54 12.934	0.183	-03 00 55.158	0.182
7.b <sup>d</sup>	...	...	...	...	...	...	...	...
7.c	04 54 11.105	0.012	-03 01 26.296	0.006	...	...	...	...
8	04 54 10.542	0.029	-03 01 27.061	0.019	04 54 10.577	0.182	-03 01 27.319	0.181

<sup>a</sup>Calculated with Equations 7-9 from Schinnerer et al. (2010).

<sup>b</sup>The source is obscured by a foreground cluster galaxy (MacKenzie et al. 2014).

<sup>c</sup>The diffuse structure of the source makes it difficult to determine an *HST* position.

<sup>d</sup>The galaxy is resolved into multiple substructures in the *HST* image.

<sup>e</sup>Positions are only provided for detected galaxies. A position for Gal. 7.b is not provided as its shape is highly irregular and somewhat diffuse.

NOTE—The positions of the sources on the *HST* image are determined by using a least-squares fitting algorithm to fit a 2D Gaussian to *HST* cutouts where the sources are isolated as best as possible. The uncertainties are the errors on the estimated means (i.e., not the standard deviations) of the fitted Gaussians. The *HST* images are RGB composites created using the F160W, F110W, and F814W filters as the red, green, and blue channels, respectively. ALMA source positions are determined by applying the same method to the  $-200 \text{ km s}^{-1}$  to  $200 \text{ km s}^{-1}$  moment-zero maps of the detected sources.

*HST* composite thumbnails, are shown in Figure 1. Integrated spectra for all galaxies can be found in Appendix C. The velocities of each spectrum are relative to the redshift of the respective galaxy as given in Table 3. The displayed spectra are the ones with the highest SNR over the different extraction regions for each source.

For the non-detected galaxies with  $\text{SNR} < 3$  as calculated using the above procedure, we instead use a

$1.5''$ -radius circular aperture centered at the *HST* location to extract a subcube. The sources were assumed to be unresolved, and the spectra were calculated at the pixel position that had the maximum flux density on the  $-200 \text{ km s}^{-1}$  to  $200 \text{ km s}^{-1}$  moment zero map.

For each of the galaxies (both detections and non-detections), we also checked to make sure that the contribution from the continuum was negligible. The  $-200 \text{ km s}^{-1}$  to  $200 \text{ km s}^{-1}$  channels of each spectrum

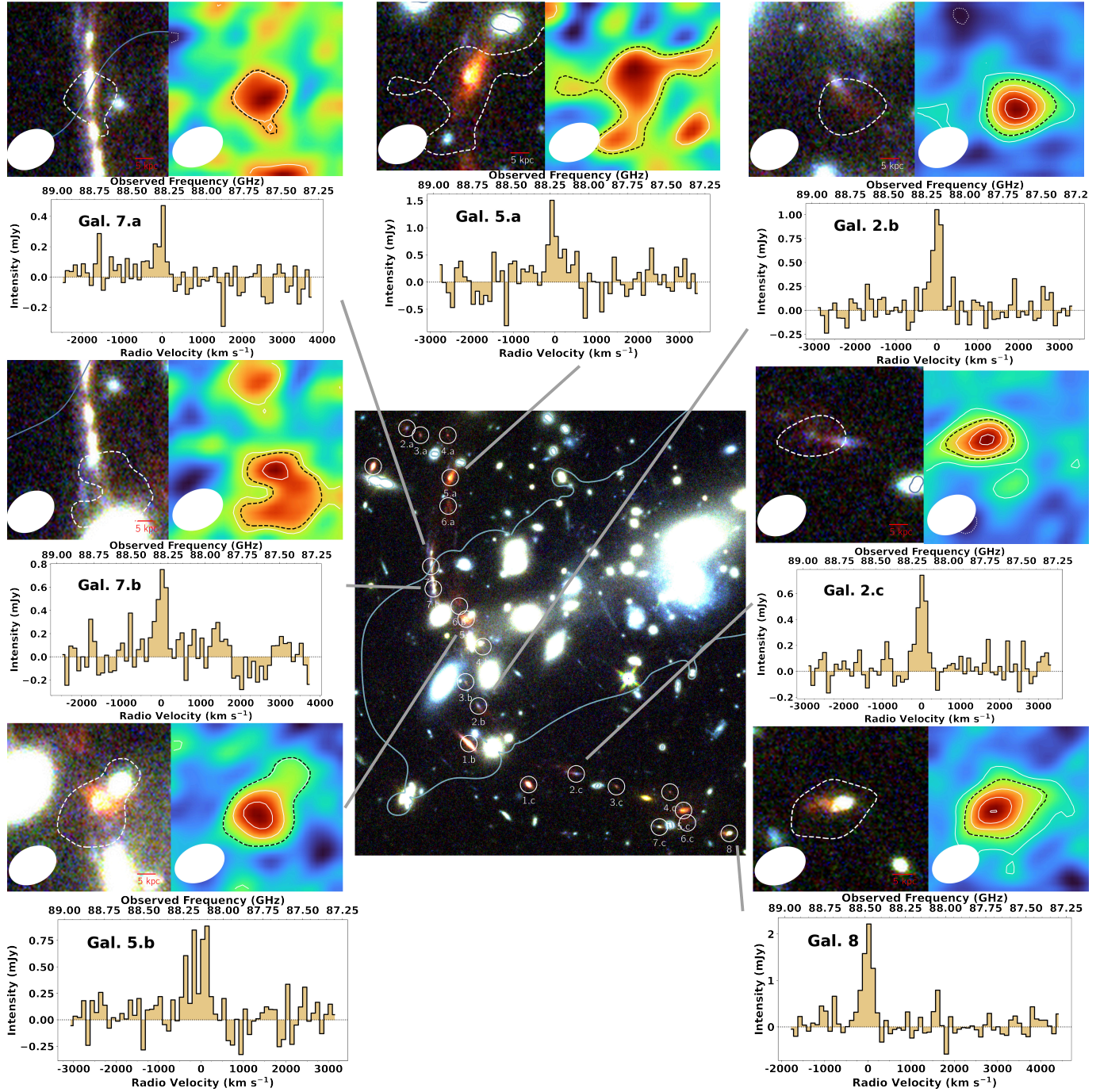


**Figure 1.** The central figure is a composite color image created using *HST* F160W, F110W, and F814W filters as the red, green, and blue channels, respectively. Overplotted in blue is the critical line of the lens model. The moment zero maps are created from the  $-200 \text{ km s}^{-1}$  to  $200 \text{ km s}^{-1}$  channels of the non-primary-beam corrected cubes. The optimized extraction regions are indicated in the corresponding moment zero maps by the dotted black line. The solid white contours start from  $2\sigma$  and go up in  $2\sigma$  increments, and the dotted contours start from  $-2\sigma$  and go in  $2\sigma$  increments, where  $\sigma$  is the rms noise. The ellipses in the bottom-left corners are the ALMA beam, which has FWHM major and minor axis sizes of  $1.810''$  and  $1.275''$  respectively, and a position angle of  $-64.3$  deg. The spectra are extracted by spatially integrating the primary-beam corrected cube within the optimized extraction regions in all channels in the spectral window. Also included are cutouts of the *HST* image with the contour corresponding to the CO extraction aperture overlaid in white. Each cutout measures  $6'' \times 6''$ , corresponding to roughly  $46 \text{ kpc} \times 46 \text{ kpc}$  on the image plane at  $z = 2.9$ . In each cutout, the up direction is north and the left direction is east.

were masked out, and the mean and rms noise of the resulting line-free spectrum were calculated. In each

**Table 2.** Star-gas offset for detected galaxies.

Gal	Offset	Position Angle	Offset	Position Angle
ID	arcsec	deg, east of north	arcsec	deg, east of north
Image plane		Source plane		
2.b	$0.96^{+0.18}_{-0.17}$	$207^{+10}_{-11}$	$0.25^{+0.11}_{-0.10}$	$98^{+11}_{-7}$
2.c	$0.99^{+0.18}_{-0.18}$	$78^{+12}_{-10}$	$0.25^{+0.12}_{-0.13}$	$93^{+11}_{-10}$
5.a	$0.30^{+0.17}_{-0.14}$	$104^{+74}_{-50}$	$0.14^{+0.11}_{-0.07}$	$95^{+147}_{-27}$
5.b	$0.70^{+0.20}_{-0.18}$	$146^{+15}_{-16}$	$0.25^{+0.07}_{-0.08}$	$80^{+14}_{-16}$
8	$0.61^{+0.18}_{-0.17}$	$117^{+18}_{-18}$	$0.33^{+0.14}_{-0.10}$	$128^{+27}_{-20}$

NOTE—The offsets and position angles are calculated from the *HST* locations to the ALMA locations (as given in Table 1). The estimates are obtained by perturbing the positions of each *HST* and ALMA pair with Gaussian noise with standard deviation equal to the position uncertainties 1000 times, calculating the offset and position angle each time, and then taking the median of the sampling distribution. The uncertainties on these estimates are difference between the median and the 16 and 84 percentile values from the sampling distributions.

case, the mean was consistent with zero (i.e., the absolute value of the mean was less than the rms noise), indicating that the continuum emission is insignificant. We also create a continuum image with the remaining three spectral windows where no spectral line emission is expected. None of the sources were detected in this continuum at  $\text{SNR} > 5$ . The mean continuum noise at the location of the sources is 0.018 mJy, and an upper limit of  $3\sigma = 0.054$  mJy would be less than 10% of the maximum flux density in each spectra (i.e., the flux density in the channel with the peak of the line). Continuum images are shown in Appendix E.

### 3.3. Molecular Gas Mass

For the detected galaxies with  $\text{SNR} > 3$ , each spectrum was fit with a 1D Gaussian model in order to obtain the  $^{12}\text{CO}(J=3\rightarrow 2)$  line flux, which was then used to calculate the molecular gas mass. In order to quantify the uncertainty in the measurement, a Monte Carlo simulation was performed. Each spectrum was perturbed with Gaussian noise, centered at the observed intensity and with a standard deviation equal to the rms noise of the signal. We then fit a Gaussian function to each of the 500 simulated spectra to obtain a distribution of best-fitting parameters.

The full width at half maximum (FWHM) for a Gaussian is related to its standard deviation  $\sigma$  by  $\text{FWHM} = 2\sqrt{2\ln 2}\sigma$ , and the line flux  $S_{\text{CO}(3\rightarrow 2)}\Delta v$  is given by the area under the Gaussian curve. This is calculated analytically as  $\sqrt{2\pi}a|\sigma|$ , where  $a$  is the peak intensity of the curve. The reported values and uncertainties for the

peak frequency, FWHM line width, and flux in Table 3 are the means and standard deviations, respectively, of the Monte Carlo realizations.

For galaxies without a strongly detected  $^{12}\text{CO}(J=3\rightarrow 2)$  emission, we derive upper limits on the line flux by assuming a boxcar line profile. The width of the profile was taken to be  $400\text{ km s}^{-1}$ , which is slightly low relative to the median detection profile width of  $512\text{ km s}^{-1}$ . The height of the profile was set at  $3\sigma$ , where  $\sigma$  is the rms noise of the 1D spectrum. The resulting  $3\sigma$  upper limits on the line fluxes for the non-detections are provided in Table 3.

We measure spectroscopic redshifts from the  $^{12}\text{CO}(J=3\rightarrow 2)$ ,  $z_{\text{CO}}$ , which are more reliable than—but largely consistent with—the redshifts provided in MacKenzie et al. (2014) based on lensing predictions. Knowing that the rest frequency of the  $^{12}\text{CO}(J=3\rightarrow 2)$  transition is  $\nu_{\text{rest}} \approx 345.796\text{ GHz}$  (Carilli & Walter 2013), we apply the equation  $\nu_{\text{obs}} = \nu_{\text{rest}}/(1+z)$ .

The intrinsic line luminosity  $L'_{\text{CO}}$  is calculated using the following equation from Solomon et al. (1992), which has been modified to include the lensing magnification:

$$L'_{\text{CO}} = \frac{c^2}{2k} \frac{S_{\text{CO}}\Delta v}{\mu} \frac{D_L^2}{\nu_{\text{obs}}^2(1+z)^3}, \quad (2)$$

where  $k = 1.381 \times 10^{-23}\text{ JK}^{-1}$  is the Boltzmann constant,  $\mu$  is the magnification of the object (with  $\mu = 1$  for unlensed sources and  $\mu > 1$  for lensed sources),  $D_L$  is the luminosity distance in Mpc, and  $\nu_{\text{obs}}$  is the observed frequency of the emission in GHz.

This  $^{12}\text{CO}(J=3\rightarrow 2)$  luminosity was converted to an equivalent  $^{12}\text{CO}(J=1\rightarrow 0)$  luminosity with an assumed rotational transition ratio of  $L'_{\text{CO}(3\rightarrow 2)}/L'_{\text{CO}(1\rightarrow 0)} = 0.5$  (Tacconi et al. 2013). The  $^{12}\text{CO}(1\rightarrow 0)$  luminosity was then used to derive the molecular gas mass. We adopt a conversion factor of  $\alpha_{\text{CO}} = 4.36\text{ M}_{\odot}/(\text{K km s}^{-1}\text{ pc}^2)$ , which accounts for the mass contribution from helium, following convention for Milky Way-like galaxies (Bolatto et al. 2013). See Section 4.5 for further discussion of the selection and uncertainty of the spectral line energy distribution (SLED) and the  $\alpha_{\text{CO}}$  conversion factor. All of the resulting values are presented in Table 3. Note that the luminosity as defined above gives the intrinsic luminosity, whereas the values reported in Table 3 are observed (i.e., lensed) luminosities.

Since the sources are gravitationally lensed, we need to take into account the amplification factor for each image due to the lensing in order to calculate the delensed (intrinsic) molecular gas mass of each source. Although the amplification factor is given with respect to the flux density, all of the calculations necessary to go from flux density to the gas mass are linear in the relevant vari-

**Table 3.** Molecular gas properties of galaxy images.

Gal	FWHM	$S_{\text{CO}(3\rightarrow 2)}\Delta v$	RMS	$z^a$	$L'_{\text{CO}(3\rightarrow 2)}$	Amplification <sup>d</sup>	Delensed $M_{\text{gas}}$	Delensed SFR <sup>d</sup>	$t_{\text{depl}}$
ID	$\text{km s}^{-1}$	$\text{Jy km s}^{-1}$	$\times 10^{-4} \text{ Jy beam}^{-1}$		$\times 10^{10} \text{ K km s}^{-1} \text{ pc}^2$		$\times 10^{10} M_{\odot}$	$M_{\odot} \text{ yr}^{-1}$	Gyr
Detections									
2.b	$260 \pm 49$	$0.305 \pm 0.038$	1.3	$2.9211 \pm 0.0005$	$1.3 \pm 0.2$	$8.1 \pm 0.4$	$1.4 \pm 0.2$	$99 \pm 9$	$0.14 \pm 0.02$
2.c	$650_{-650}^{+1131}$	$0.248 \pm 0.071$	1.0	$2.922 \pm 0.003$	$1.0 \pm 0.3$	$6.1 \pm 0.1$	$1.5 \pm 0.4$	$99 \pm 9$	$0.15 \pm 0.04$
5.a	$446 \pm 264$	$0.503 \pm 0.150$	3.2	$2.919 \pm 0.001$	$2.1 \pm 0.6$	$5.3 \pm 0.1$	$3.4 \pm 1.0$	$< 35$	$< 0.98$
5.b	$712_{-712}^{+992}$	$0.438 \pm 0.088$	2.0	$2.923 \pm 0.002$	$1.8 \pm 0.4$	$6.4 \pm 0.1$	$2.5 \pm 0.5$	$< 35$	$< 0.71$
7.a	$982 \pm 890$	$0.155 \pm 0.064$	1.0	$2.910 \pm 0.006$	$0.6 \pm 0.3$	$33.0 \pm 2.0$	$0.2 \pm 0.1$	$11 \pm 2$	$0.15 \pm 0.07$
7.b	$513 \pm 487$	$0.278 \pm 0.090$	1.6	$2.916 \pm 0.001$	$1.2 \pm 0.4$	$45.0 \pm 3.0$	$0.2 \pm 0.1$	$11 \pm 2$	$0.20 \pm 0.08$
8	$273 \pm 34$	$0.633 \pm 0.069$	2.6	$2.9065 \pm 0.0002$	$2.6 \pm 0.3$	$1.73 \pm 0.04$	$13.1 \pm 1.5$	$290 \pm 40$	$0.45 \pm 0.08$
Non-Detections									
1.a	...	$< 0.424$	3.6	$2.92233_{-0.00010}^{+0.00013}$ <sup>b</sup>	$< 1.7$	$3.8 \pm 0.06$	$< 3.9$	$4 \pm 1$ <sup>e</sup>	...
1.b	...	$< 0.195$	1.6	$2.92233_{-0.00010}^{+0.00013}$ <sup>b</sup>	$< 0.8$	$20.0 \pm 1.0$	$< 0.3$	$4 \pm 1$ <sup>e</sup>	...
1.c	...	$< 0.195$	1.6	$2.92233_{-0.00010}^{+0.00013}$ <sup>b</sup>	$< 0.8$	$7.3 \pm 0.1$	$< 1.0$	$4 \pm 1$ <sup>e</sup>	...
2.a	...	$< 0.634$	5.3	$2.91 \pm 0.04$	$< 2.7$	$2.86 \pm 0.04$	$< 8.0$	$99 \pm 9$	$< 0.81$
3.a	...	$< 0.475$	4.0	$2.94 \pm 0.04$	$< 2.0$	$3.19 \pm 0.05$	$< 5.4$	$< 23$	...
3.b	...	$< 0.222$	1.9	$2.94 \pm 0.04$	$< 0.9$	$2.98 \pm 0.05$	$< 2.7$	$< 23$	...
3.c	...	$< 0.259$	2.2	$2.94 \pm 0.04$	$< 1.1$	$4.31 \pm 0.08$	$< 2.2$	$< 23$	...
4.a	...	$< 0.364$	3.0	$2.94 \pm 0.04$	$< 1.5$	$3.57 \pm 0.06$	$< 3.7$	$< 50$	...
4.b	...	$< 0.231$	1.9	$2.94 \pm 0.04$	$< 1.0$	$6.2 \pm 0.2$	$< 1.3$	$< 50$	...
4.c	...	$< 0.299$	2.5	$2.94 \pm 0.04$	$< 1.3$	$3.36 \pm 0.06$	$< 3.2$	$< 50$	...
5.c	...	$< 0.334$	2.8	$2.89 \pm 0.03$	$< 1.4$	$2.89 \pm 0.04$	$< 4.2$	$< 35$	...
6.a	...	$< 0.364$	3.0	$2.86 \pm 0.03$	$< 1.5$	$8.2 \pm 0.2$	$< 1.6$	$53 \pm 14$	$< 0.30$
6.b	...	$< 0.267$	2.2	$2.86 \pm 0.03$	$< 1.1$	$4.98 \pm 0.08$	$< 1.9$	$53 \pm 14$	$< 0.36$
6.c	...	$< 0.323$	2.7	$2.86 \pm 0.03$	$< 1.4$	$2.76 \pm 0.04$	$< 4.2$	$53 \pm 14$	$< 0.80$
7.c	...	$< 0.338$	2.8	$2.911 \pm 0.003$ <sup>c</sup>	$< 1.4$	$2.87 \pm 0.04$	$< 4.2$	$11 \pm 2$	$< 3.86$

<sup>a</sup> Redshifts for the detections are calculated from the CO detections. Redshifts for the non-detections are redshifts derived from the lensing model of MacKenzie et al. (2014) unless otherwise specified.

<sup>b</sup> Median  $z_{\text{spec}}$  derived from VLT/X-SHOOTER spectrum of Gal. 1.b (Man et al. submitted). The quoted lower and upper uncertainties are the differences between the median and the 16 and 84 percentiles, respectively.

<sup>c</sup> This is a spectroscopic redshift from Borys et al. (2004), derived from interstellar absorption lines.

<sup>d</sup> From MacKenzie et al. (2014) unless otherwise specified.

<sup>e</sup> Median SFR of Gal. 1.b from Man et al. submitted, adjusted to magnification  $\mu = 20$  from MacKenzie et al. (2014). The quoted lower and upper uncertainties are the differences between the median and the 16 and 84 percentiles, respectively.

NOTE—Table of values for the detections (top portion of the table) and non-detections (bottom portion). The delensed gas masses and star formation rates are lensing-corrected values. The rest of the data are observed values. Unless otherwise specified, values given with uncertainties are the means and standard deviations from Monte Carlo simulations. Upper limits are  $3\sigma$  upper limits.

ables. Thus, we can directly apply the amplification factor to calculate the delensed gas mass.

We are aware of the revised lens model for the foreground cluster presented in Jauzac et al. (2020), which would impact both the SFR and the molecular gas mass. For consistency in the magnification factors used for  $M_{\text{gas}}$  and SFR and to ensure that the depletion times are not affected by magnification, we choose to use the original magnifications as given in MacKenzie et al. (2014). We note that although both  $M_{\text{gas}}$  and SFR are based on luminosities ( $L'_{\text{CO}}$  and  $L_{\text{IR}}$  respectively), the scaling due to the change in magnification may not be equal between the two. This is due to the offsets between the CO emission and the SFR tracers, as described in Section

3.2. The different regions may be magnified differently by the foreground cluster, and thus one luminosity may be magnified more strongly than the other. We do not consider the effects of differential lensing in our analysis.

### 3.4. Spectrum Stacking

Each galaxy in the group, apart from Gal. 8, has three multiple images. We stack the spectra from the three multiple images in an attempt to increase the SNR. Each of the spectra are normalized by their respective magnifications (MacKenzie et al. 2014) so that the more strongly lensed sources do not inadvertently contribute more to the stacked result. In order to reduce the importance of noisier spectra, the stacking was done with



an inverse-variance weighting (where the variances are also corrected for magnification), according to Equation 3:

$$\mathbf{S}_s = \frac{1}{\sum_{i=1}^3 \frac{1}{\text{Var}(\mathbf{S}_i)}} \sum_{i=1}^3 \frac{1}{\text{Var}(\mathbf{S}_i)} \mathbf{S}_i, \quad (3)$$

where the index  $i = 1, 2, 3$  corresponds to the "a", "b", and "c" multiple images respectively,  $\mathbf{S}_i$  is the  $i^{\text{th}}$  de-lensed spectrum (i.e.,  $\mathbf{S}_i = \mathbf{s}_i/\mu_i$  where  $\mathbf{s}_i$  is the  $i^{\text{th}}$  observed spectrum),  $\text{Var}(\mathbf{S}_i)$  is the variance of the  $i^{\text{th}}$  de-lensed spectrum, and  $\mathbf{S}_s$  is the stacked spectrum. The first term in the equation is a normalization term to ensure that the weights sum to 1.

For Gals. 2, 5, and 7, the stacking procedure increased the SNR over the maximum SNR of the constituent spectra (e.g., max SNR among Gals. 2.a, 2.b, and 2.c) by only a marginal amount. Furthermore, stacking the non-detected galaxies where none of the constituent sources were detected did not bring them over the  $\text{SNR} > 3$  threshold.

As with the constituent sources, the stacked spectra are classified as a detection if  $\text{SNR} > 3$ , and the Gaussian fits are used to calculate the flux. Otherwise, a boxcar profile is used to estimate an upper limit for the flux in the same procedure as described in Section 3.3. The resulting gas properties derived from the stacked spectra are presented in Table 4.

## 4. DISCUSSION

### 4.1. Star Formation in High Redshift Galaxies

The molecular gas and the star formation rate are in essence the amount of fuel available to a galaxy and the galaxy's fuel consumption rate. The ratio between the two quantities provides an estimate for the molecular gas depletion time, which is the time that a galaxy will take to consume all of its currently available fuel at its present SFR, assuming there are no other causes of net change in the molecular gas mass.

Figure 2 shows the SFR as a function of molecular gas mass for the galaxies from this work, as well as from a compiled sample of over 500 galaxies, the majority of which are CO-detected. This compilation is presented in Table 5 in Appendix A. The compilation includes normal galaxies and starbursts in various environments up to  $z = 5.3$ . The emphasis lies on the high-redshift (using  $z > 1$  as the cutoff) normal galaxy population where the sources in this work belong. The only included study which does not target CO emission is Zavala et al. (2019), which presents dust continuum observations. However, this study provides a

useful and relatively large sample of high-redshift normal protocluster galaxies as a point of comparison. For starbursts where the infrared (IR) luminosity was given instead of the SFR, Equation 4 from Kennicutt (1998) was used to calculate the SFR (Ivison et al. 2011; Papadopoulos et al. 2012; Combes et al. 2013; Magdis et al. 2014; Herrero-Illana et al. 2019). All SFRs are scaled to a Kroupa (2001) IMF following the conversion factors provided in Madau & Dickinson (2014)—to convert from a Salpeter IMF, multiply by 0.67, and to convert from a Chabrier IMF, multiply by 0.67/0.63.

In Figure 2, we separate the compilation into three populations:  $z < 1$  normal galaxies,  $z < 1$  starbursts, and  $z > 1$  galaxies. We do not distinguish between normal galaxies and starbursts for the  $z > 1$  population as there is not as clear of a distinction between the two populations.

We find that most of the galaxies from this work lie on the lower end, both in terms of SFR and  $M_{\text{gas}}$ , of the region of the plot that is most densely populated by other  $z > 1$  galaxies—clustered around the 1 Gyr line, with  $M_{\text{gas}} > 10^{10} M_{\odot}$ . However, most of the detections have depletion times closer to 0.1 – 0.5 Gyr (see Table 3). The shorter depletion times of these galaxies indicate that they may quench before  $z = 2.4$ , which is roughly 0.5 Gyr after  $z = 2.9$ . By  $z = 2$ , 1 Gyr will have elapsed, and most of the sources will have depleted their molecular gas reservoir.

The outlier of most interest is Gal. 7 because its SFR and gas mass are lower than the bulk of the other  $z > 1$  galaxies by an order of magnitude. It is the source at the highest magnification, with the "b" image being magnified by a factor of  $45 \pm 3$ , and without lensing, more telescope time than is practical would be required in order to achieve the same SNR as in the presented spectrum. We also note that all of our limits are upper limits, and the true location of the undetected galaxies in the  $M_{\text{gas}} - \text{SFR}$  parameter space is toward the position of Gal. 7, with lower masses and SFRs than other high-redshift detections.

There is a span of two orders of magnitude in the star formation rates of the galaxies in this work, ranging from  $3.8_{-0.92}^{+0.98} M_{\odot} \text{yr}^{-1}$  for Gal. 1 (Man et al., submitted) to  $290 \pm 90 M_{\odot} \text{yr}^{-1}$  for Gal. 8 (MacKenzie et al. 2014). This is comparable to what is observed by Zavala et al. (2019), who find SFRs from as low as  $6_{-5}^{+23} M_{\odot} \text{yr}^{-1}$  to as high as  $612_{-200}^{+280} M_{\odot} \text{yr}^{-1}$  in  $z \approx 2.1$  and  $z \approx 2.5$  protocluster galaxies. Although sensitivity and selection bias play a large role at high redshifts (e.g., selections based on narrow-band filters bias against galaxies with low star-formation activity, and due to the  $M_{*} - \text{SFR}$  relation for typical galaxies, against low mass

**Table 4.** Properties of stacked galaxy images.

Gal	FWHM	$S_{\text{CO}(3\rightarrow 2)}\Delta v^a$	RMS	$z_{\text{CO}}$	$L'_{\text{CO}(3\rightarrow 2)}$	Delensed $M_{\text{gas}}$	$t_{\text{depl}}$
ID	$\text{km s}^{-1}$	$\text{mJy km s}^{-1}$	$\times 10^{-4} \text{ Jy/beam}$		$\times 10^9 \text{ K km s}^{-1} \text{ pc}^2$	$\times 10^{10} M_{\odot}$	Gyr
Detections							
2	$279 \pm 33$	$37.705 \pm 3.625$	0.13	$2.9210 \pm 0.0004$	$1.58 \pm 0.15$	$1.36 \pm 0.13$	$0.14 \pm 0.01$
5	$694 \pm 143$	$83.385 \pm 12.426$	0.34	$2.921 \pm 0.001$	$3.50 \pm 0.52$	$3.01 \pm 0.45$	$< 0.86$
7	$379 \pm 362$	$4.317 \pm 0.975$	0.02	$2.915 \pm 0.001$	$0.18 \pm 0.04$	$0.16 \pm 0.04$	$0.14 \pm 0.03$
Non-Detections							
1	...	$< 9.429$	0.08	...	$< 0.39$	$< 0.34$	...
3	...	$< 50.107$	0.42	...	$< 2.12$	$< 1.82$	...
4	...	$< 33.357$	0.28	...	$< 1.41$	$< 1.21$	...
6	...	$< 35.120$	0.29	...	$< 1.47$	$< 1.26$	$< 0.24$

<sup>a</sup>Note that the units are in  $\text{mJy km s}^{-1}$  rather than  $\text{Jy km s}^{-1}$  as in Table 3.

NOTE—Properties derived from the stacked spectra. Values are all delensed/intrinsic values as the constituent spectra (eg. Gal 2.a, 2.b, and 2.c) have all been divided by their respective amplifications before the stacking procedure. Stacking was done with a inverse-variance weighted sum. The top section of the table provides values for the galaxies where two or more of the multiple images were detected in  $^{12}\text{CO}(J=3\rightarrow 2)$ . In these cases, the flux of the stacked spectrum was calculated with a Gaussian fitting procedure as described in Section 3.3. The rest of the galaxies' fluxes are calculated using a boxcar profile, also described in Section 3.3. The reported upper limits for these galaxies are  $3\sigma$  upper limits.

galaxies (Muldreu et al. 2015)), the few confirmed protocluster galaxies at  $z > 3$  with CO detections form stars much more vigorously than the galaxies in this work. For example, the protoclusters from Miller et al. (2018) and Oteo et al. (2018) have total SFRs exceeding  $6000 M_{\odot} \text{ yr}^{-1}$ .

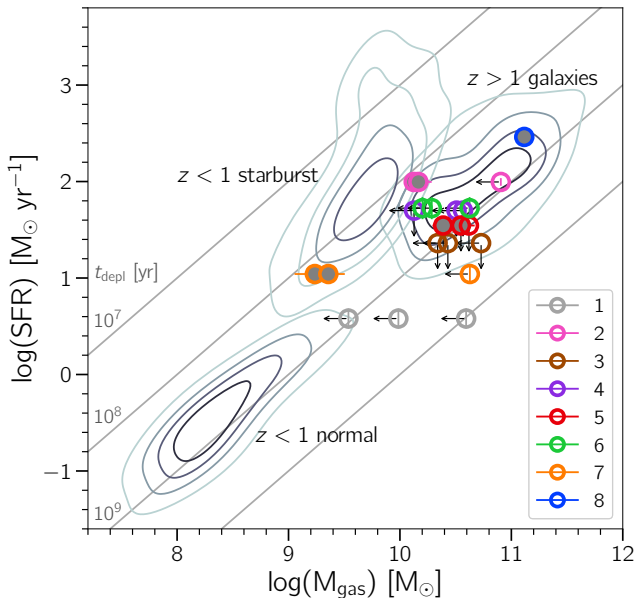
The large range of SFRs at  $z = 1$  to 3—and possibly at even higher redshifts, but there are too few detections to say with certainty—suggest that protocluster galaxies are quenched during the  $z = 1$  to 3 period. During this period, we concurrently see starburst galaxies with high SFRs and post-starburst galaxies with nearly no star formation. It is possible that the quenching of protocluster galaxies is aided by the dense environments—promoting more interactions which could lead to quenching (Lotz et al. 2013)—in which these galaxies reside. If indeed galaxies in dense environments are more rapidly quenched than field galaxies, a high fraction of quiescent galaxies would be observed in dense environments at  $z < 1$ . Existing studies on the impact of the environment on quenching support this (Cooper et al. 2007; Wang et al. 2018; Strazzullo et al. 2019; Castignani et al. 2020). Preferential quenching in dense environments would also mean that the more strongly star forming galaxies would be in the field at later cosmic epochs. This is supported by the inversion in the density-SFR relation at  $z \approx 1$ , showing that locally, galaxies with high SFRs are preferentially found in isolated environments (Dressler 1980; Gomez et al. 2003; Cooper et al.

2007; Elbaz et al. 2007; Tran et al. 2010; Popesso et al. 2015a,b).

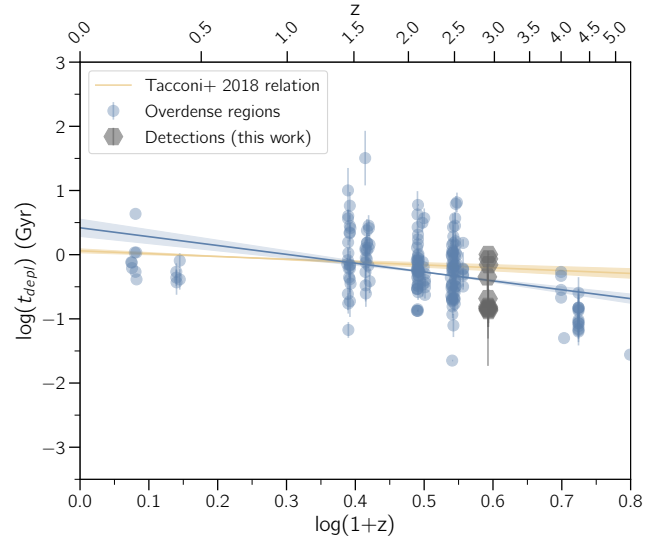
#### 4.2. Dependence of Depletion Time on Redshift

Figure 3 shows the redshift-evolution of the depletion time, distinguished by the environment. The data are from compiled galaxies in Table 5, where studies are marked as "overdense" if they provide measurements of (proto-)cluster galaxies. The blue line is the fit to galaxies in overdense environments, and the blue shading is the  $1\sigma$  confidence interval on that fit. The fit and uncertainty are calculated from the sample means and the standard errors of the line parameters as determined by the Levenberg-Marquardt algorithm for 10,000 bootstrapped samples (Levenberg 1944; Efron 1979). Also plotted in yellow for comparison is the field scaling relation for CO measurements from Tacconi et al. (2018). The depletion time here is given by  $\log(t_{\text{depl}}) = (0.06 \pm 0.03) - (0.44 \pm 0.13) \log(1 + z) - (0.43 \pm 0.03) \log(\delta\text{MS}) + (0.17 \pm 0.04)(\log M_* - 10.7)$ . This scaling relation is for CO measurements, and is informed by 667 galaxies. The normalization factors we assume for this relation are  $\delta\text{MS} = 1$  and  $\log M_* = 10.7$ , where  $\delta\text{MS} = \text{sSFR}/\text{sSFR}(\text{MS}, z, M_*)$  is the offset from the star formation main sequence (MS). These are chosen so that the relation is only dependent on redshift. Although the depletion time depends on main-sequence offset and stellar mass (the  $C_t$  and  $D_t$  coefficients in Tacconi et al. 2018), we do not consider these factors due to a lack of adequate data for accurate measurements.

Looking at the evolution of the depletion time of galaxies, the fit suggests that high-redshift galaxies have shorter depletion times than lower redshift galaxies. For galaxies in overdense environments, the slope of the best-fit line is  $t_{\text{depl}} \propto (1+z)^{-1.37 \pm 0.26}$ . We note here that there may be biases against long depletion times observationally and/or in the sample we have compiled, which cannot be accounted for in the line fitting. We compare this to the Tacconi et al. (2018) field relation of  $t_{\text{depl}} \propto (1+z)^{-0.44 \pm 0.13}$ , which is less steep, suggesting that while depletion time decreases with increasing redshift for all galaxies, the evolution is stronger for galaxies in overdense environments. Darvish et al. (2018) also investigated the redshift evolution of depletion time for galaxies in various environmental densities up to  $z \approx 3.5$  and found that the depletion time decreases with increasing redshift. However, they did not



**Figure 2.** Star formation rate (SFR) as a function of molecular gas mass, plotted in log-log scale. All SFRs have been scaled to a Kroupa (2001) IMF. A compilation of literature measurements listed in Table 5 is separated into three galaxy populations as labeled. These are shown as contours corresponding to levels of constant density (in the probabilistic sense). The contours shown here are at 20%, 40%, 60%, and 80%, indicating the probability mass below/outside the contour. The darker inner contours indicate the parameter space that a larger number of galaxies occupy. Galaxies from this work are plotted separately; detections are plotted with grey face colours, and non-detections are plotted as rings. The ring colour indicates the source galaxy as given by the legend in the lower-right corner. For all galaxies except for Gal. 8, there are three points, one for each of the multiple images. Diagonal grey lines indicate constant depletion time ( $t_{\text{depl}} = M_{\text{gas}}/\text{SFR}$ ) as annotated in grey text.



**Figure 3.** Depletion time  $t_{\text{depl}} = M_{\text{gas}}/\text{SFR}$  in Gyr as a function of redshift, plotted in log-log scale. The blue line and shading indicate the line of best fit and the corresponding  $1\sigma$  uncertainty from 10,000 bootstrapped samples of galaxies in overdense environments (see Table 5). The yellow line is the field scaling relation from Tacconi et al. (2018), where only the impact of redshift is considered. The depletion time here is given by  $\log(t_{\text{depl}}) = (0.06 \pm 0.03) - (0.44 \pm 0.13) \log(1+z) - (0.43 \pm 0.03) \log(\delta\text{MS}) + (0.17 \pm 0.04)(\log M_* - 10.7)$ , and we assume normalization factors of  $\delta\text{MS} = 1$  and  $\log M_* = 10.7$  so that redshift is the only factor influencing the depletion time.

find evidence for a dependence of the redshift-depletion time relation on environmental density.

#### 4.3. Dependence of Depletion Time on Environmental Density

In line with other studies, we find that galaxies in overdense environments at  $z < 2$  have depletion times that are roughly consistent with (Noble et al. 2017; Rudnick et al. 2017; Darvish et al. 2018) the depletion times of coeval field galaxies, as determined by field scaling relations (from Tacconi et al. 2013, 2018 or Genzel et al. 2015). This is in spite of the fact that high-redshift cluster galaxies have similar or larger gas fractions compared to coeval field galaxies (Noble et al. 2017; Hayashi et al. 2018), suggesting that galaxies in overdense environments are less efficient at converting gas into stars. We also note that the stellar mass is likely an important factor in the efficacy of these environmental processes.

From the fit shown in Figure 3 (which includes many starburst galaxies), galaxies in overdense environments seem to have shorter depletion times than field galaxies at  $z > 2.5$ . However, this fit is informed by mostly  $z < 2.5$  galaxies, many of which are starbursts. If we analyze the small subset of CO-detected galaxies at  $z > 2.5$

with normal SFRs, this becomes unclear. In the [Tacconi et al. \(2018\)](#) sample, only four detections belong to this subset: one non-lensed Lyman break galaxy from [Magdis et al. \(2012\)](#) (M23), and three lensed galaxies from [Saintonge et al. \(2013\)](#) (cB58, 8:00arc, and Eye). The mean depletion time for these four galaxies is  $0.21 \pm 0.04$  Gyr. From the compilation, there are 23 galaxies with normal SFRs in overdense environments with known depletion times—19 from [Tadaki et al. \(2019\)](#) and [Wang et al. \(2018\)](#), and 5 from this work (Gals. 2.b, 2.c, 7.a, 7.b, and 8). The mean depletion time for these 23 galaxies is longer, at  $1.14 \pm 0.14$  Gyr. Based on this very small sample, it would seem then, that even at high redshifts, the depletion times of galaxies in overdense environments are longer than those of galaxies in field environments.

The primary problem preventing consensus in this discussion is the scarcity of CO-detected galaxies at  $z > 2.5$  with normal star formation rates, both in the field and in overdense environments. Current studies of molecular gas, particularly those with CO, at high-redshift are primarily composed of massive starbursts (e.g., [Riechers et al. 2010a](#); [Bothwell et al. 2013](#); [Oteo et al. 2018](#); [Miller et al. 2018](#)). More observations of high-redshift normal galaxies are needed in order to better constrain the relationship between redshift and depletion time, and to identify the impact of the environment on that relationship.

#### 4.4. Star-Gas Offset

We find *HST*-ALMA spatial offsets of  $0.14 - 0.33''$  on the source plane, corresponding to  $1.1 - 2.6$  kpc at  $z = 2.9$ . Such offsets are not particularly surprising given the conditions of our sources, and have also been observed in other high-redshift galaxies ([Carilli et al. 2010](#); [Daddi et al. 2010](#); [Hodge et al. 2013](#)). Galaxies at high redshift are dustier than their local counterparts ([Hodge & da Cunha 2020](#)). It is conceivable that in our case the dust is co-spatial with the CO emissions, and obscures a large portion of UV emission from the galaxies. The spatial offset would only be exacerbated by interactions between galaxies—which are more likely to happen in overdense environments—as they could cause gas and dust to be flung out in a way that it becomes extended and/or offset relative to the stars in galaxies ([Zwicky 1956](#); [Barnes & Hernquist 1992](#)).

The multiply-imaged nature of the lensed sources lends further evidence that the observed offset is intrinsic rather than due to the astrometry. Consider Gals. 2.b and 2.c, two of the most strongly detected sources with SNRs of 6.4 and 5.8 respectively. Figure 1 in this work and Figure 1 from [MacKenzie et al. \(2014\)](#) show

that the offset is mirrored across the critical line. The velocity gradients in the moment one maps, which are calculated with the equation

$$M_1 = \frac{\int I v dv}{\int I dv}, \quad (4)$$

where  $I$  is the intensity of the pixel value in Jy and  $v$  is the velocity of the channel in  $\text{km s}^{-1}$ , and the integration goes across the  $-200 \text{ km s}^{-1}$  to  $200 \text{ km s}^{-1}$  velocity channels for each pixel in the optimal extraction region (see Section 3.2), are also mirrored across the critical line (see Figure 4). Moment one maps of all detected galaxies are given in Appendix D. A closer look at the *HST* images also reveals that the CO emission is co-spatial with diffuse, red blobs of dust near each source in all the images. If in fact the offset was due to astrometry, we would not expect to see any of these things; rather, the offset would be of a similar magnitude and direction in all the sources.

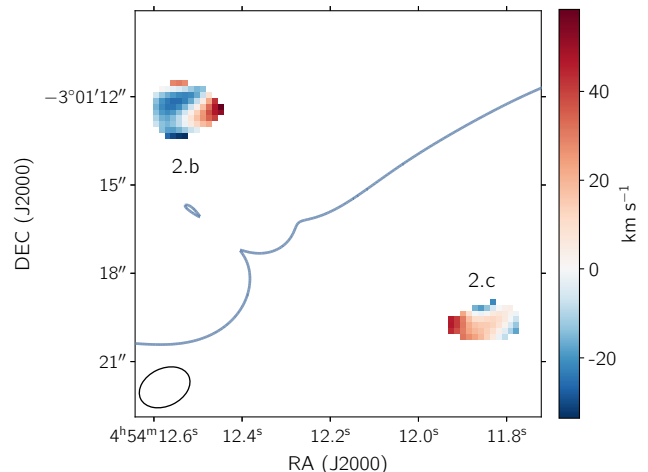


**Figure 4.** Moment one map of Gal. 2.b (left) and 2.c (right), as created from data cubes masked to only retain the optimal extraction region (see Section 3.2 for details) of each source, plotted together with the critical line of the lens model. A velocity gradient of approximately  $80 \text{ km s}^{-1}$  is present in both sources, and the directional alignment of the gradient in Gal. 2.b appears to be mirrored across the critical line relative to that of Gal. 2.c. The velocities are given relative to the systematic velocity of the respective sources. The black elliptical ring in the bottom left corner indicate the ALMA beam.

#### 4.5. Systematic Uncertainties in the Gas Mass

The measurement of the molecular gas mass relies on two factors, both of which carry significant systematic uncertainties. The first is the ratio between the strengths of the different CO rotational transitions, or

the CO SLED. The  $^{12}\text{CO}(J=3\rightarrow 2)$  transition requires more energy to be excited than the ground-state transition, and thus it traces denser clumps of gas with higher temperatures (Riechers et al. 2007). A conversion factor  $r_{3\rightarrow 2/1\rightarrow 0} = L'_{\text{CO}(3\rightarrow 2)}/L'_{\text{CO}(1\rightarrow 0)}$  needs to be used in order to infer the  $^{12}\text{CO}(J=1\rightarrow 0)$  luminosity. However, a wide range of values have been adopted in literature, ranging from 0.4 – 1.15 in  $z \approx 2.5$  galaxies (Ivison et al. 2011; Gómez-Guijarro et al. 2019). This conversion factor is also increasingly impacted by the cosmic microwave background (CMB) at high redshifts (da Cunha et al. 2013); the elevated CMB in the early Universe reduces the brightness contrast of CO line emissions against background emissions (Zhang et al. 2016). Across all redshifts, the value most commonly adopted or calculated by the studies in our compilation targeting that transition is 0.5. This is the value we use for our calculations.

The second major uncertainty is the CO-to- $\text{H}_2$  conversion factor,  $\alpha_{\text{CO}}$ . This conversion factor is dependent on many physical properties like the metallicity and the pressure of the interstellar medium (ISM) (Genzel et al. 2012; Carilli & Walter 2013; Dessauges-Zavadsky et al. 2017). This is particularly problematic at high redshifts and in low-mass galaxies where there is a rapid metallicity evolution (Tan et al. 2013). Even within the Milky Way and nearby spirals where resolved observations are easier to obtain and ISM properties are better understood,  $\alpha_{\text{CO}}$  is not certain, with Bolatto et al. (2013) finding a factor of two scatter. For extragalactic sources, it is much more difficult to determine  $\alpha_{\text{CO}}$ . For Milky Way-like galaxies, a value of  $\alpha_{\text{CO}} = 4.36 \text{ M}_{\odot} (\text{K km s}^{-1} \text{ pc}^{-2})$  is commonly used, and for (U)LIRGs and SMGs,  $\alpha_{\text{CO}} = 0.8$  is commonly used (Downes & Solomon 1998; Dessauges-Zavadsky et al. 2015; Noble et al. 2019). If metallicity measurements are available, it may be beneficial to adopt a CO line intensity and metallicity dependent  $\alpha_{\text{CO}}$  factor from the best-fitting function in Narayanan et al. (2012) rather than the conventional bimodal  $\alpha_{\text{CO}}$  values, as this has been shown to significantly reduce scatter in star formation relations.

Together, the CO SLED and  $\alpha_{\text{CO}}$  factors introduce close to an order of magnitude in systematic uncertainty into the  $M_{\text{gas}}$  and  $t_{\text{depl}}$  derived in this work.

#### 4.6. Future Prospects

Future observations of these sources and other lensed high-redshift galaxies could take many avenues. Future instruments like the Next Generation Very Large Array (ngVLA) and ALMA Band 1 will enable large, multi-transition CO surveys of more representative galaxies

at  $z > 2$ , which would open up the possibility to model the CO SLED (e.g., Narayanan & Krumholz (2014)). Higher spatial resolution observations would allow for virial mass estimates that could be used to independently constrain  $\alpha_{\text{CO}}$ , and to reconstruct the gas distribution on the source plane (e.g., Brewer & Lewis 2006; Riechers et al. 2007; Vegetti & Koopmans 2009; Spingola et al. 2020).

It is conceivable that the overdense environment is more conducive to mergers and active galactic nuclei (AGN) activity. Radio counterparts to some of the sources in this work have been identified by Berciano Alba et al. (2010) (e.g., "RJ Bright" near Gal 1.b and the three multiple images of the "E" system near the three multiple images of Gals. 5 and 6). These could be indications of the existence of potential mergers and/or AGN in the galaxies. We examined the spectra for broader CO components, but the ALMA data at hand are not sufficiently deep to identify signatures of AGN-driven molecular gas outflows. Future investigations into the presence of AGN could shed light on its impact on star formation in protocluster galaxies.

Follow-up rest-frame optical imaging could also aim to provide information about the stellar mass of the galaxies of this  $z = 2.9$  group. That would allow for the calculation of gas fractions in these galaxies, which could lead to further understanding of the impact of the environment on molecular gas. Stellar masses could also be used to compare the sources to the star formation main sequence, allowing for a more comprehensive understanding of star formation in these galaxies.

## 5. CONCLUSIONS

In this paper, we have presented a study of a gravitationally lensed group of galaxies at  $z = 2.9$ . With a compact ALMA configuration, we target the  $^{12}\text{CO}(J=3\rightarrow 2)$  emission line and spectroscopically confirm the redshifts of seven images of four members. These molecular gas mass measurements represent the highest redshift CO detections in dense environments for galaxies that are not undergoing extreme starburst. We compile a diverse sample of over 500 galaxies up to  $z = 5.3$  in order to place our results in context. We find that the galaxies in this work are consistent in molecular gas mass and SFR with the high-redshift ( $z > 1$ ) normal population from our compilation. The inferred molecular gas masses of our detections span a range of  $(0.2 - 13.1) \times 10^{10} \text{ M}_{\odot}$ .

We also investigated the impact of the environment on the depletion time of galaxies. The sources in this work are among the highest redshift CO-detected galaxies with normal star formation rates in an overdense environment, and extend the discussion about the impact

of the environment beyond  $z = 2.5$ . At the same time, our results highlight the challenge of constraining molecular gas relations for normal galaxies at high-redshift due to the scarcity of observations. We find that at high redshifts, galaxies tend to have shorter depletion times than those at low redshifts, and that this depletion time evolution is steeper for galaxies in overdense environments than for field galaxies. At  $z > 2.5$ , we find tentative evidence that those in overdense environments have shorter depletion times than coeval field galaxies, but this does not seem to hold when considering only CO-detected galaxies with normal star formation rates. The lack of CO detections of normal galaxies at  $z > 2.5$  makes it difficult to conclusively determine the impact of the environment on the depletion time. Further investigation into cluster evolution will be needed in order to fully understand how early galaxies in dense environments evolve.

#### ACKNOWLEDGEMENTS

We thank the anonymous referee for a careful reading of this manuscript and for providing helpful suggestions. The Dunlap Institute is funded through an endowment established by the David Dunlap family and the University of Toronto. The University of Toronto operates on the traditional land of the Huron-Wendat, the Seneca, and most recently, the Mississaugas of the Credit River; J.S. and A.M. are grateful to have the opportunity to work on this land. This paper makes use of data from ALMA program

ADS/JAO.ALMA#2017.1.00616.S. ALMA is a partnership of ESO (representing its member states), NSF (USA) and NINS (Japan), together with NRC (Canada) and NSC and ASIAA (Taiwan) and KASI (Republic of Korea), in cooperation with the Republic of Chile. The Joint ALMA Observatory is operated by ESO, AUI/NRAO and NAOJ. J.Z. acknowledges support from ANR grant ANR-17-CE31-0017 (3DGasFlows). We acknowledge Sune Toft, Harald Ebeling, Desika Narayanan, and Justin Spilker for their contributions to earlier stages of this work.

*Software:* NumPy (van der Walt et al. 2011), spectral-cube (Ginsburg et al. 2019), Matplotlib (Hunter 2007), Astropy (Robitaille et al. 2013; Price-Whelan et al. 2018), seaborn (Waskom & the seaborn development team 2020), SciPy (Virtanen et al. 2020), CASA (McMullin et al. 2007), grizli (Brammer 2019)

#### AUTHOR CONTRIBUTIONS

J.S. performed the data analysis, created the figures, wrote most of the paper, and made revisions under the supervision of A.M. A.M. designed the study, led the writing of the ALMA proposal, configured and processed the ALMA observations, and wrote Section 2. J.Z. contributed to the design of the study. Z.Z. contributed to the ALMA imaging. J.Z., Z.Z., and M.S. provided feedback on the ALMA proposal. G.B. processed the *HST* images. J.R. performed the lens model inversion. All authors participated in scientific discussions and provided comments which led to revisions of the paper both prior to and following submission.

#### REFERENCES

- Barnes, J. E., & Hernquist, L. 1992, *ARA&A*, 30, 705, doi: [10.1146/annurev.aa.30.090192.003421](https://doi.org/10.1146/annurev.aa.30.090192.003421)
- Berciano Alba, A., Garrett, M. A., Koopmans, L. V. E., & Wucknitz, O. 2007, *A&A*, 462, 903, doi: [10.1051/0004-6361:20065223](https://doi.org/10.1051/0004-6361:20065223)
- Berciano Alba, A., Koopmans, L. V. E., Garrett, M. A., Wucknitz, O., & Limousin, M. 2010, *Astronomy and Astrophysics*, 509, A54, doi: [10.1051/0004-6361/200912903](https://doi.org/10.1051/0004-6361/200912903)
- Blanton, M. R., & Moustakas, J. 2009, *Annual Review of Astronomy and Astrophysics*, 47, 159–210, doi: [10.1146/annurev-astro-082708-101734](https://doi.org/10.1146/annurev-astro-082708-101734)
- Bolatto, A. D., Wolfire, M., & Leroy, A. K. 2013, *Annual Review of Astronomy and Astrophysics*, 51, 207–268, doi: [10.1146/annurev-astro-082812-140944](https://doi.org/10.1146/annurev-astro-082812-140944)
- Borys, C., Chapman, S., Donahue, M., et al. 2004, *Monthly Notices of the Royal Astronomical Society*, 352, 759–767, doi: [10.1111/j.1365-2966.2004.07982.x](https://doi.org/10.1111/j.1365-2966.2004.07982.x)
- Bothwell, M. S., Smail, I., Chapman, S. C., et al. 2013, *MNRAS*, 429, 3047, doi: [10.1093/mnras/sts562](https://doi.org/10.1093/mnras/sts562)
- Brammer, G. 2019, Grizli: Grism redshift and line analysis software. <http://ascl.net/1905.001>
- Brewer, B. J., & Lewis, G. F. 2006, *The Astrophysical Journal*, 637, 608–619, doi: [10.1086/498409](https://doi.org/10.1086/498409)
- Carilli, C., & Walter, F. 2013, *Annual Review of Astronomy and Astrophysics*, 51, 105, doi: [10.1146/annurev-astro-082812-140953](https://doi.org/10.1146/annurev-astro-082812-140953)
- Carilli, C. L., Daddi, E., Riechers, D., et al. 2010, *The Astrophysical Journal*, 714, 1407–1417, doi: [10.1088/0004-637x/714/2/1407](https://doi.org/10.1088/0004-637x/714/2/1407)

- Castignani, G., Combes, F., Salomé, P., & Freundlich, J. 2020, *Astronomy & Astrophysics*, 635, A32, doi: [10.1051/0004-6361/201936148](https://doi.org/10.1051/0004-6361/201936148)
- Chambers, K. C., Magnier, E. A., Metcalfe, N., et al. 2019, *The Pan-STARRS1 Surveys*. <https://arxiv.org/abs/1612.05560>
- Cicone, C., Bothwell, M., Wagg, J., et al. 2017, *Astronomy & Astrophysics*, 604, A53, doi: [10.1051/0004-6361/201730605](https://doi.org/10.1051/0004-6361/201730605)
- Ciesla, L., Béthermin, M., Daddi, E., et al. 2020, *Astronomy & Astrophysics*, 635, A27, doi: [10.1051/0004-6361/201936727](https://doi.org/10.1051/0004-6361/201936727)
- Combes, F., García-Burillo, S., Braine, J., et al. 2013, *Astronomy & Astrophysics*, 550, A41, doi: [10.1051/0004-6361/201220392](https://doi.org/10.1051/0004-6361/201220392)
- Combes, F., Rex, M., Rawle, T. D., et al. 2012, *Astronomy & Astrophysics*, 538, L4, doi: [10.1051/0004-6361/201118750](https://doi.org/10.1051/0004-6361/201118750)
- Cooper, M. C., Newman, J. A., Weiner, B. J., et al. 2007, *Monthly Notices of the Royal Astronomical Society*, 383, 1058–1078, doi: [10.1111/j.1365-2966.2007.12613.x](https://doi.org/10.1111/j.1365-2966.2007.12613.x)
- Coppin, K. E. K., Swinbank, A. M., Neri, R., et al. 2007, *The Astrophysical Journal*, 665, 936–943, doi: [10.1086/519789](https://doi.org/10.1086/519789)
- Cybulski, R., Yun, M. S., Erickson, N., et al. 2016, *Monthly Notices of the Royal Astronomical Society*, 459, 3287–3306, doi: [10.1093/mnras/stw798](https://doi.org/10.1093/mnras/stw798)
- da Cunha, E., Groves, B., Walter, F., et al. 2013, *The Astrophysical Journal*, 766, 13, doi: [10.1088/0004-637x/766/1/13](https://doi.org/10.1088/0004-637x/766/1/13)
- Daddi, E., Bournaud, F., Walter, F., et al. 2010, *The Astrophysical Journal*, 713, 686–707, doi: [10.1088/0004-637x/713/1/686](https://doi.org/10.1088/0004-637x/713/1/686)
- Daddi, E., Dannerbauer, H., Liu, D., et al. 2015, *Astronomy & Astrophysics*, 577, A46, doi: [10.1051/0004-6361/201425043](https://doi.org/10.1051/0004-6361/201425043)
- Danielson, A. L. R., Swinbank, A. M., Smail, I., et al. 2010, *Monthly Notices of the Royal Astronomical Society*, no–no, doi: [10.1111/j.1365-2966.2010.17549.x](https://doi.org/10.1111/j.1365-2966.2010.17549.x)
- Dannerbauer, H., Lehnert, M. D., Emonts, B., et al. 2017, *Astronomy & Astrophysics*, 608, A48, doi: [10.1051/0004-6361/201730449](https://doi.org/10.1051/0004-6361/201730449)
- Darvish, B., Scoville, N. Z., Martin, C., et al. 2018, *The Astrophysical Journal*, 860, 111, doi: [10.3847/1538-4357/aac836](https://doi.org/10.3847/1538-4357/aac836)
- Dessauges-Zavadsky, M., Zamojski, M., Schaerer, D., et al. 2015, *Astronomy & Astrophysics*, 577, A50, doi: [10.1051/0004-6361/201424661](https://doi.org/10.1051/0004-6361/201424661)
- Dessauges-Zavadsky, M., Zamojski, M., Rujopakarn, W., et al. 2017, *Astronomy & Astrophysics*, 605, A81, doi: [10.1051/0004-6361/201628513](https://doi.org/10.1051/0004-6361/201628513)
- Downes, D., & Solomon, P. M. 1998, *The Astrophysical Journal*, 507, 615–654, doi: [10.1086/306339](https://doi.org/10.1086/306339)
- Dressler, A. 1980, *ApJ*, 236, 351, doi: [10.1086/157753](https://doi.org/10.1086/157753)
- Efron, B. 1979, *The Annals of Statistics*, 7, 1. <http://www.jstor.org/stable/2958830>
- Egami, E., Rex, M., Rawle, T. D., et al. 2010, *A&A*, 518, L12, doi: [10.1051/0004-6361/201014696](https://doi.org/10.1051/0004-6361/201014696)
- Elbaz, D., Daddi, E., Le Borgne, D., et al. 2007, *Astronomy & Astrophysics*, 468, 33–48, doi: [10.1051/0004-6361:20077525](https://doi.org/10.1051/0004-6361:20077525)
- Gaia Collaboration, Brown, A. G. A., Vallenari, A., et al. 2018, *A&A*, 616, A1, doi: [10.1051/0004-6361/201833051](https://doi.org/10.1051/0004-6361/201833051)
- Geach, J. E., Smail, I., Moran, S. M., et al. 2011, *The Astrophysical Journal*, 730, L19, doi: [10.1088/2041-8205/730/2/119](https://doi.org/10.1088/2041-8205/730/2/119)
- Genzel, R., Tacconi, L. J., Combes, F., et al. 2012, *The Astrophysical Journal*, 746, 69, doi: [10.1088/0004-637x/746/1/69](https://doi.org/10.1088/0004-637x/746/1/69)
- Genzel, R., Tacconi, L. J., Lutz, D., et al. 2015, *ApJ*, 800, 20, doi: [10.1088/0004-637X/800/1/20](https://doi.org/10.1088/0004-637X/800/1/20)
- Ginsburg, A., Koch, E., Robitaille, T., et al. 2019, *radio-astro-tools/spectral-cube: v0.4.4, v0.4.4*, Zenodo, doi: [10.5281/zenodo.2573901](https://doi.org/10.5281/zenodo.2573901)
- Gomez, P. L., Nichol, R. C., Miller, C. J., et al. 2003, *The Astrophysical Journal*, 584, 210–227, doi: [10.1086/345593](https://doi.org/10.1086/345593)
- Gómez-Guijarro, C., Riechers, D. A., Pavesi, R., et al. 2019, *ApJ*, 872, 117, doi: [10.3847/1538-4357/ab002a](https://doi.org/10.3847/1538-4357/ab002a)
- Hayashi, M., Tadaki, K.-i., Kodama, T., et al. 2018, *The Astrophysical Journal*, 856, 118, doi: [10.3847/1538-4357/aab3e7](https://doi.org/10.3847/1538-4357/aab3e7)
- Herrero-Illana, R., Privon, G. C., Evans, A. S., et al. 2019, *Astronomy & Astrophysics*, 628, A71, doi: [10.1051/0004-6361/201834088](https://doi.org/10.1051/0004-6361/201834088)
- Hodge, J. A., Carilli, C. L., Walter, F., Daddi, E., & Riechers, D. 2013, *The Astrophysical Journal*, 776, 22, doi: [10.1088/0004-637x/776/1/22](https://doi.org/10.1088/0004-637x/776/1/22)
- Hodge, J. A., & da Cunha, E. 2020. <https://arxiv.org/abs/2004.00934>
- Högbom, J. A. 1974, *A&AS*, 15, 417
- Hunter, J. D. 2007, *Matplotlib: A 2D graphics environment*, IEEE COMPUTER SOC, doi: [10.1109/MCSE.2007.55](https://doi.org/10.1109/MCSE.2007.55)
- Iverson, R. J., Papadopoulos, P. P., Smail, I., et al. 2011, *Monthly Notices of the Royal Astronomical Society*, 412, 1913, doi: [10.1111/j.1365-2966.2010.18028.x](https://doi.org/10.1111/j.1365-2966.2010.18028.x)
- Jauzac, M., Klein, B., Kneib, J.-P., et al. 2020, 22, 1. <https://arxiv.org/abs/2006.10700>

- Kennicutt, R. C. 1998, *Annual Review of Astronomy and Astrophysics*, 36, 189–231, doi: [10.1146/annurev.astro.36.1.189](https://doi.org/10.1146/annurev.astro.36.1.189)
- Kroupa, P. 2001, *Monthly Notices of the Royal Astronomical Society*, 322, 231–246, doi: [10.1046/j.1365-8711.2001.04022.x](https://doi.org/10.1046/j.1365-8711.2001.04022.x)
- Lee, M. M., Tanaka, I., Kawabe, R., et al. 2017, *The Astrophysical Journal*, 842, 55, doi: [10.3847/1538-4357/aa74c2](https://doi.org/10.3847/1538-4357/aa74c2)
- Levenberg, K. 1944, *Quarterly of Applied Mathematics*, 2, 164, doi: [10.1090/qam/10666](https://doi.org/10.1090/qam/10666)
- Lotz, J. M., Papovich, C., Faber, S. M., et al. 2013, *ApJ*, 773, 154, doi: [10.1088/0004-637X/773/2/154](https://doi.org/10.1088/0004-637X/773/2/154)
- MacKenzie, T. P., Scott, D., Smail, I., et al. 2014, *Monthly Notices of the Royal Astronomical Society*, 445, 201, doi: [10.1093/mnras/stu1623](https://doi.org/10.1093/mnras/stu1623)
- Madau, P., & Dickinson, M. 2014, *Annual Review of Astronomy and Astrophysics*, 52, 415–486, doi: [10.1146/annurev-astro-081811-125615](https://doi.org/10.1146/annurev-astro-081811-125615)
- Magdis, G. E., Daddi, E., Sargent, M., et al. 2012, *ApJL*, 758, L9, doi: [10.1088/2041-8205/758/1/L9](https://doi.org/10.1088/2041-8205/758/1/L9)
- Magdis, G. E., Rigopoulou, D., Hopwood, R., et al. 2014, *The Astrophysical Journal*, 796, 63, doi: [10.1088/0004-637x/796/1/63](https://doi.org/10.1088/0004-637x/796/1/63)
- Man, A., & Belli, S. 2018, *Nature Astronomy*, 2, 695–697, doi: [10.1038/s41550-018-0558-1](https://doi.org/10.1038/s41550-018-0558-1)
- McMullin, J. P., Waters, B., Schiebel, D., Young, W., & Golap, K. 2007, in *Astronomical Society of the Pacific Conference Series*, Vol. 376, *Astronomical Data Analysis Software and Systems XVI*, ed. R. A. Shaw, F. Hill, & D. J. Bell, 127
- Miller, T. B., Chapman, S. C., Aravena, M., et al. 2018, in *Nature*, doi: [10.1038/s41586-018-0025-2](https://doi.org/10.1038/s41586-018-0025-2)
- Mo, H., van den Bosch, F. C., & White, S. 2010, *Galaxy Formation and Evolution*
- Muldrew, S. I., Hatch, N. A., & Cooke, E. A. 2015, *Monthly Notices of the Royal Astronomical Society*, 452, 2528–2539, doi: [10.1093/mnras/stv1449](https://doi.org/10.1093/mnras/stv1449)
- Murphy, E. J., Condon, J. J., Schinnerer, E., et al. 2011, *ApJ*, 737, 67, doi: [10.1088/0004-637X/737/2/67](https://doi.org/10.1088/0004-637X/737/2/67)
- Narayanan, D., & Krumholz, M. R. 2014, *MNRAS*, 442, 1411, doi: [10.1093/mnras/stu834](https://doi.org/10.1093/mnras/stu834)
- Narayanan, D., Krumholz, M. R., Ostriker, E. C., & Hernquist, L. 2012, *Monthly Notices of the Royal Astronomical Society*, 421, 3127–3146, doi: [10.1111/j.1365-2966.2012.20536.x](https://doi.org/10.1111/j.1365-2966.2012.20536.x)
- Noble, A. G., McDonald, M., Muzzin, A., et al. 2017, *The Astrophysical Journal*, 842, L21, doi: [10.3847/2041-8213/aa77f3](https://doi.org/10.3847/2041-8213/aa77f3)
- Noble, A. G., Muzzin, A., McDonald, M., et al. 2019, *The Astrophysical Journal*, 870, 56, doi: [10.3847/1538-4357/aaf1c6](https://doi.org/10.3847/1538-4357/aaf1c6)
- Oteo, I., Ivison, R. J., Dunne, L., et al. 2018, *ApJ*, 856, 72, doi: [10.3847/1538-4357/aaa1f1](https://doi.org/10.3847/1538-4357/aaa1f1)
- Papadopoulos, P. P., van der Werf, P. P., Xilouris, E. M., et al. 2012, *Monthly Notices of the Royal Astronomical Society*, 426, 2601, doi: [10.1111/j.1365-2966.2012.21001.x](https://doi.org/10.1111/j.1365-2966.2012.21001.x)
- Popesso, P., Biviano, A., Finoguenov, A., et al. 2015a, *Astronomy & Astrophysics*, 574, A105, doi: [10.1051/0004-6361/201424711](https://doi.org/10.1051/0004-6361/201424711)
- . 2015b, *Astronomy & Astrophysics*, 579, A132, doi: [10.1051/0004-6361/201424715](https://doi.org/10.1051/0004-6361/201424715)
- Price-Whelan, A. M., Sipőcz, B. M., Günther, H. M., et al. 2018, *The Astropy Project: Building an Open-science Project and Status of the v2.0 Core Package*, *American Astronomical Society*, doi: [10.3847/1538-3881/aabc4f](https://doi.org/10.3847/1538-3881/aabc4f)
- Riechers, D. A., Carilli, C. L., Walter, F., & Momjian, E. 2010a, *The Astrophysical Journal*, 724, L153–L157, doi: [10.1088/2041-8205/724/2/1153](https://doi.org/10.1088/2041-8205/724/2/1153)
- Riechers, D. A., Walter, F., Carilli, C. L., et al. 2007, in *Astronomical Society of the Pacific Conference Series*, Vol. 375, *From Z-Machines to ALMA: (Sub)Millimeter Spectroscopy of Galaxies*, ed. A. J. Baker, J. Glenn, A. I. Harris, J. G. Mangum, & M. S. Yun, 148
- Riechers, D. A., Capak, P. L., Carilli, C. L., et al. 2010b, *The Astrophysical Journal*, 720, L131–L136, doi: [10.1088/2041-8205/720/2/1131](https://doi.org/10.1088/2041-8205/720/2/1131)
- Robitaille, T. P., Tollerud, E. J., Greenfield, P., et al. 2013, *Astropy: A community Python package for astronomy*, *EDP Sciences*, doi: [10.1051/0004-6361/201322068](https://doi.org/10.1051/0004-6361/201322068)
- Rudnick, G., Hodge, J., Walter, F., et al. 2017, *The Astrophysical Journal*, 849, 27, doi: [10.3847/1538-4357/aa87b2](https://doi.org/10.3847/1538-4357/aa87b2)
- Saintonge, A., Lutz, D., Genzel, R., et al. 2013, *The Astrophysical Journal*, 778, 2, doi: [10.1088/0004-637x/778/1/2](https://doi.org/10.1088/0004-637x/778/1/2)
- Schinnerer, E., Sargent, M. T., Bondi, M., et al. 2010, *ApJS*, 188, 384, doi: [10.1088/0067-0049/188/2/384](https://doi.org/10.1088/0067-0049/188/2/384)
- Schmidt, M. 1959, *ApJ*, 129, 243, doi: [10.1086/146614](https://doi.org/10.1086/146614)
- Shapley, A. E. 2011, *Annual Review of Astronomy and Astrophysics*, 49, 525–580, doi: [10.1146/annurev-astro-081710-102542](https://doi.org/10.1146/annurev-astro-081710-102542)
- Solomon, P. M., Downes, D., & Radford, S. J. E. 1992, *The Astrophysical Journal*, 398, L29, doi: [10.1086/186569](https://doi.org/10.1086/186569)
- Spilker, J. S., Aravena, M., Marrone, D. P., et al. 2015, *The Astrophysical Journal*, 811, 124, doi: [10.1088/0004-637x/811/2/124](https://doi.org/10.1088/0004-637x/811/2/124)



- Spingola, C., McKean, J. P., Vegetti, S., et al. 2020, *Monthly Notices of the Royal Astronomical Society*, 495, 2387–2407, doi: [10.1093/mnras/staa1342](https://doi.org/10.1093/mnras/staa1342)
- Stach, S. M., Swinbank, A. M., Smail, I., et al. 2017, *The Astrophysical Journal*, 849, 154, doi: [10.3847/1538-4357/aa93f6](https://doi.org/10.3847/1538-4357/aa93f6)
- Strazzullo, V., Pannella, M., Mohr, J. J., et al. 2019, *Astronomy & Astrophysics*, 622, A117, doi: [10.1051/0004-6361/201833944](https://doi.org/10.1051/0004-6361/201833944)
- Tacconi, L. J., Genzel, R., & Sternberg, A. 2020. <https://arxiv.org/abs/2003.06245>
- Tacconi, L. J., Neri, R., Genzel, R., et al. 2013, *The Astrophysical Journal*, 768, 74, doi: [10.1088/0004-637X/768/1/74](https://doi.org/10.1088/0004-637X/768/1/74)
- Tacconi, L. J., Genzel, R., Saintonge, A., et al. 2018, *The Astrophysical Journal*, 853, 179, doi: [10.3847/1538-4357/aaa4b4](https://doi.org/10.3847/1538-4357/aaa4b4)
- Tadaki, K., Iono, D., Yun, M. S., et al. 2018, *Nature*, 560, 613, doi: [10.1038/s41586-018-0443-1](https://doi.org/10.1038/s41586-018-0443-1)
- Tadaki, K.-i., Kodama, T., Hayashi, M., et al. 2019, *Publications of the Astronomical Society of Japan*, 71, 1, doi: [10.1093/pasj/psz005](https://doi.org/10.1093/pasj/psz005)
- Tan, Q., Daddi, E., Sargent, M., et al. 2013, *The Astrophysical Journal*, 776, L24, doi: [10.1088/2041-8205/776/2/L24](https://doi.org/10.1088/2041-8205/776/2/L24)
- Tran, K.-V. H., Papovich, C., Saintonge, A., et al. 2010, *The Astrophysical Journal*, 719, L126–L129, doi: [10.1088/2041-8205/719/2/L126](https://doi.org/10.1088/2041-8205/719/2/L126)
- van der Walt, S., Colbert, S. C., & Varoquaux, G. 2011, *The NumPy Array: A Structure for Efficient Numerical Computation*, *Institute of Electrical and Electronics Engineers (IEEE)*, doi: [10.1109/mcse.2011.37](https://doi.org/10.1109/mcse.2011.37)
- Vegetti, S., & Koopmans, L. V. E. 2009, *Monthly Notices of the Royal Astronomical Society*, 392, 945–963, doi: [10.1111/j.1365-2966.2008.14005.x](https://doi.org/10.1111/j.1365-2966.2008.14005.x)
- Virtanen, P., Gommers, R., Oliphant, T. E., et al. 2020, *Nature Methods*, 17, 261, doi: <https://doi.org/10.1038/s41592-019-0686-2>
- Walter, F., Carilli, C., Bertoldi, F., et al. 2004, *The Astrophysical Journal*, 615, L17–L20, doi: [10.1086/426017](https://doi.org/10.1086/426017)
- Wang, T., Elbaz, D., Daddi, E., et al. 2018, *The Astrophysical Journal*, 867, L29, doi: [10.3847/2041-8213/aab2c](https://doi.org/10.3847/2041-8213/aab2c)
- Waskom, M., & the seaborn development team. 2020, *mwaskom/seaborn*, latest, Zenodo, doi: [10.5281/zenodo.592845](https://doi.org/10.5281/zenodo.592845)
- Zavala, J. A., Casey, C. M., Scoville, N., et al. 2019, *The Astrophysical Journal*, 887, 183, doi: [10.3847/1538-4357/ab5302](https://doi.org/10.3847/1538-4357/ab5302)
- Zhang, Z.-Y., Papadopoulos, P. P., Ivison, R. J., et al. 2016, *Royal Society Open Science*, 3, 160025, doi: [10.1098/rsos.160025](https://doi.org/10.1098/rsos.160025)
- Zitrin, A., Broadhurst, T., Barkana, R., Rephaeli, Y., & Benítez, N. 2010, *Monthly Notices of the Royal Astronomical Society*, no–no, doi: [10.1111/j.1365-2966.2010.17574.x](https://doi.org/10.1111/j.1365-2966.2010.17574.x)
- Zwicky, F. 1956, *Ergebnisse der exakten Naturwissenschaften*, 29, 344

## APPENDIX

## A. COMPILATION

**Table 5.** Comparison sample, ordered by maximum redshift.

Reference	Overdense	Starburst	Objects	Redshift Range	Gas Mass Range	SFR Range	Depletion Time Range
					$\times 10^{10} M_{\odot}$	$M_{\odot} \text{ yr}^{-1}$	Gyr
Cicone et al. (2017)	no	no	97	0.011 – 0.029	0.005 – 1.046	0 – 13	0.004 – 3.238
Herrero-Illana et al. (2019) <sup>a</sup>	no	yes	53	0.011 – 0.088	0.090 – 3.017	20 – 450	0.016 – 0.183
Papadopoulos et al. (2012) <sup>a</sup>	no	yes	70	0.003 – 0.100	0.005 – 1.392	15 – 286	0.007 – 1.684
Cybulski et al. (2016)	yes	no	8	0.187 – 0.208	0.92 – 1.84	3 – 44	0.412 – 4.325
Geach et al. (2011)	yes	no	5	0.380 – 0.396	1.38 – 5.06	37 – 66	0.371 – 0.806
Magdis et al. (2014) <sup>a</sup>	no	yes	9	0.216 – 0.436	0.52 – 1.56	71 – 898	0.014 – 0.107
Combes et al. (2013) <sup>a</sup>	no	yes	39	0.607 – 0.996	0.08 – 3.36	201 – 5535	0.001 – 0.050
Hayashi et al. (2018)	yes	no	17	1.445 – 1.471	2.7 – 10.7	3 – 154	0.443 – 10.030
Stach et al. (2017)	yes	yes	6	1.450 – 1.472	1.0 – 2.4	43 – 149	0.067 – 0.414
Daddi et al. (2010, 2015)	no	no	6	1.414 – 1.600	4.2 – 12.0	66 – 425	0.282 – 0.703
Rudnick et al. (2017)	yes	no	2	1.624 – 1.629	3.31 – 11.22	12 – 165	0.678 – 2, 595
Noble et al. (2017, 2019)	yes	no	17	1.596 – 1.635	1.7 – 25.5	3 – 230	0.248 – 31.970
Dannerbauer et al. (2017)	yes	no	1	2.148	18.0	372	0.484
Tacconi et al. (2013)	no	no	53	1.002 – 2.434	1.1 – 35.0	18 – 670	0.146 – 3.436
Iverson et al. (2011) <sup>a</sup>	no	yes	5	2.201 – 2.487	2.5 – 9.8	568 – 1430	0.029 – 0.130
Lee et al. (2017)	yes	no	7	2.478 – 2.487	3.14 – 18.52	69 – 440	0.079 – 3.699
Zavala et al. (2019)	yes	no	67	2.085 – 2.513	1.5 – 37.3	3 – 670	0.022 – 5.955
Wang et al. (2018)	yes	no	14	2.494 – 2.515	1.4 – 55.0	14 – 796	0.200 – 6.170
Tadaki et al. (2019)	yes	no	16	2.144 – 2.529	5.75 – 34.67	38 – 496	0.211 – 6.521
Gómez-Guijarro et al. (2019)	yes	yes	11	2.171 – 2.602	6.61 – 109.65	106 – 1808	0.236 – 1.525
Riechers et al. (2010b) <sup>b</sup>	no	no	2	2.730 – 3.070	0.046 – 0.093	27 – 149	0.006 – 0.017
Coppin et al. (2007) <sup>b</sup>	no	no	1	3.074	0.24	25	0.095
Saintonge et al. (2013) <sup>b</sup>	no	no	10	1.411 – 3.074	0.56 – 40.74	19 – 647	0.119 – 1.024
Spingola et al. (2020) <sup>b</sup>	no	yes	2	2.059 – 3.200	25.0 – 34.0	415 – 542	0.461 – 0.820
Dessauges-Zavadsky et al. (2015, 2017) <sup>b</sup>	no	no	7	1.585 – 3.631	0.3 – 7.4	10 – 81	0.076 – 1.254
Oteo et al. (2018)	yes	yes	4	4.000 – 4.000	10.8 – 26.2	200 – 1224	0.214 – 0.539
Carilli et al. (2010) <sup>b</sup>	yes	yes	1	4.050	16.0	3190	0.050
Tan et al. (2013)	no	no	2	3.216 – 4.058	16.0 – 18.0	181 – 330	0.485 – 0.996
Miller et al. (2018) <sup>b</sup>	yes	yes	14	4.300 – 4.300	1.0 – 12.0	68 – 1304	0.063 – 0.254
Riechers et al. (2010a)	yes	yes	1	5.298	5.3	1914	0.028

<sup>a</sup>Star formation rates for these studies are calculated from the IR luminosity using the Kennicutt (1998) relation.

<sup>b</sup>Source galaxies are gravitationally lensed.

NOTE—All galaxies are CO-detected except for Zavala et al. (2019). All star formation rates have been scaled to the Kroupa (2001) IMF following the factors given in Madau & Dickinson (2014).

## B. MOMENT ZERO MAPS

Below is an example of a moment zero map. The full figure set containing moment zero maps for all galaxies (22 images) is available in the online version of the paper.

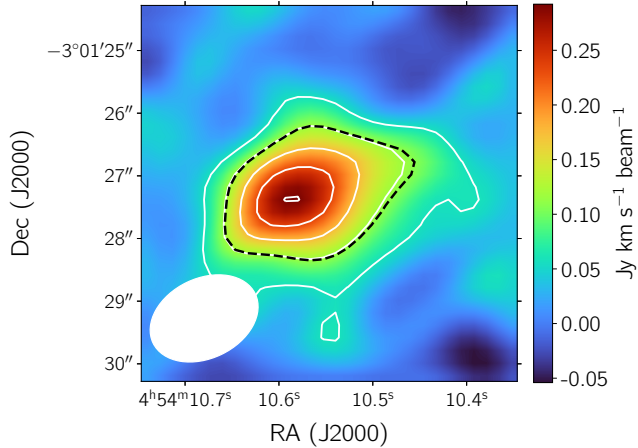


**Figure 5.** Moment zero map of Gal. 8 centered on the *HST* position. The image is created from the  $-200 \text{ km s}^{-1}$  to  $200 \text{ km s}^{-1}$  channels of the non-primary-beam corrected data cubes, and measures  $6'' \times 6''$ . The solid white contours start from  $2\sigma$  and go up in  $2\sigma$  increments, and the dotted contours start from  $-2\sigma$  and go in  $2\sigma$  increments, where  $\sigma$  is the rms noise. The ellipses in the bottom-left corners are the ALMA beam, which has FWHM major and minor axis sizes of  $1.810''$  and  $1.275''$  respectively, and a position angle of  $-64.3 \text{ deg}$ . The optimized extraction regions are indicated by the dotted black line. The full figure set with the moment zero maps for all galaxies (22 images) is provided in the online version of the paper.

## C. INTEGRATED SPECTRA

Below is an example of an integrated spectrum. The full figure set containing spectra for all galaxies (22 images) is available in the online version of the paper.

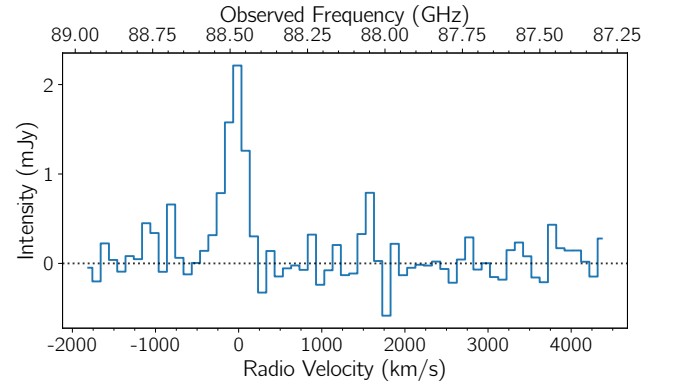


**Figure 6.** Integrated spectrum of Gal. 8, created by spatially integrating the primary-beam corrected cube in all channels in the spectral window. The integration region is determined by the optimal extraction region (see Section 3.2 for details).

## D. MOMENT ONE MAPS

Below is an example of a moment one map. The full figure set containing moment one maps for the detected galaxies (7 images) is available in the online version of the paper.

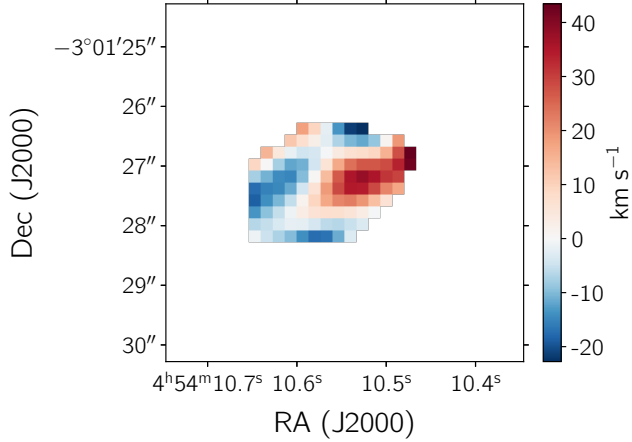


**Figure 7.** Moment one map of Gal. 8, as created from a data cube masked to only retain the optimal extraction region (see Section 3.2 for details) in the  $-200 \text{ km s}^{-1}$  to  $200 \text{ km s}^{-1}$  channels of the non-primary-beam corrected cubes. The velocities are given relative to the systematic velocity of the source.

## E. CONTINUUM IMAGES

Below is an example of a continuum image. The full figure set containing continuum images for all galaxies (22 images) is available in the online version of the paper.

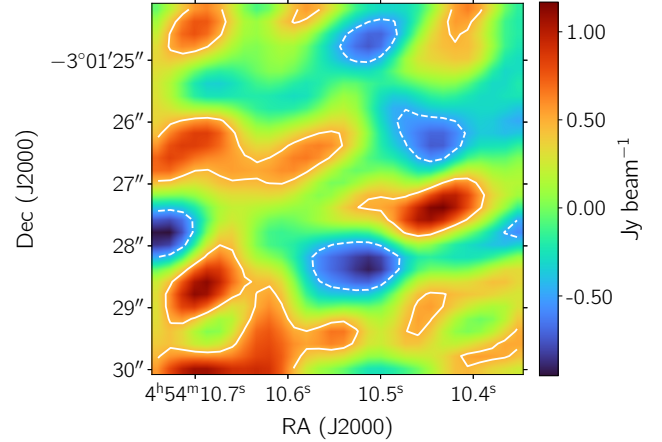


**Figure 8.** Continuum image of Gal. 8, centered on the *HST* position and measuring  $6'' \times 6''$ . The continuum image is created with the three spectral windows where no spectral line emission is expected. The contours indicate the rms noise, with the solid contours starting at  $1\sigma$  and increasing in  $2\sigma$  increments, and the dashed contours starting at  $-1\sigma$  and decreasing in  $2\sigma$  increments.